the infected cell. Thus, the cell-to-cell transmission can be categorized into two manners based on the state of infecting viruses, either *cell-free* or cell-associated virions.

Influenza virus, belonging to the family of *Orthomyxoviridae*, is one of the most serious zoonotic pathogens and causes seasonal epidemics or periodic pandemics among human beings around the world. The viral envelope consists of a lipid bilayer derived from cells that anchors three of viral transmembrane proteins, hemagglutinin (HA), neuraminidase (NA), and matrix protein 2 (M2). Influenza virus infection is initiated by the attachment of HA on virus particles to cell surface receptors containing sialic acids [12]. It has been known that the specific interaction between HA and sialic acid species is one of the determinants of the host range of influenza viruses [13]. Beside its role in the viral attachment, HA is also involved in intracellular fusion between viral envelope and host cell endosome membrane in the endocytotic pathway, by which the virus content is released inside the host cell [14]. The functional maturation of HA is mediated by the cleavage of HA into two disulfide-linked glycopolypeptides, HA1 and HA2 [15], accomplished by trypsin or trypsin-like proteases derived from host cells [16–19]. The membrane fusion is induced by a conformational change in the mature HA, which is triggered at low pH in the endosome, allowing viral ribonucleoprotein complexes to release into the cytoplasm [20,21]. Thus, HA plays a critical role in initiation and progression of influenza virus infection. Influenza virus NA possesses the enzymatic activity that cleaves α-ketosidic linkages between terminal sialic acids and adjacent sugar residues of cellular glycoconjugates [22]. The sialidase activity of NA removes terminal sialic acid residues from HA and NA proteins as well as host cell surface glycoproteins. Since the terminal sialic acid of sialyloligosaccharides is critical for HA binding, the receptor-destroying activity of NA serves to counter the receptor-binding activity of HA. It is quite likely that this activity contributes to prevention of successive superinfection of an infected cell [23]. In the absence of the functional sialidase activity, progeny virions aggregate on the cell surface due to the HA receptor-binding activity and can not be released [24,25]. Thus, NA cleaves sialic acids from the cell surface and facilitates virus release from infected cells. However, it is not clear whether every progeny virion is released as *cell-free* virion to infect the uninfected cells after diffusion into the extracellular environment. Influenza viruses are generally transmitted as *cell-free* viruses from infected to uninfected cell but they may also infect through the cell-to-cell transmission, in particular during local lesion formation.

Here, we examined whether influenza virus transmits from an infected cell to adjacent uninfected cells without virus release. Live cell imaging techniques showed that a recombinant influenza virus, in which the *NA* gene was replaced with the *green fluorescence protein* gene, spreads from an infected cell to adjacent cells forming infected cell clusters. Furthermore, progeny virions remain associated on the surface of infected cell even after budding, and then progeny virions could be passed to adjacent uninfected cells.

Results

Influenza virus can spread in an NA-independent manner to adjacent cells

To examine the transmission pathway of influenza virus, we performed immunofluorescence analyses by using anti-nucleoprotein (NP) polyclonal antibody. Influenza virus can form an infection center even in the presence of oseltamivir, a potent NA inhibitor (commercially known as Tamiflu) [26–28]. Oseltamivir at the concentration of 50 μg/ml completely prevented the release of progeny influenza viruses (Figure 1A). Noted that a large

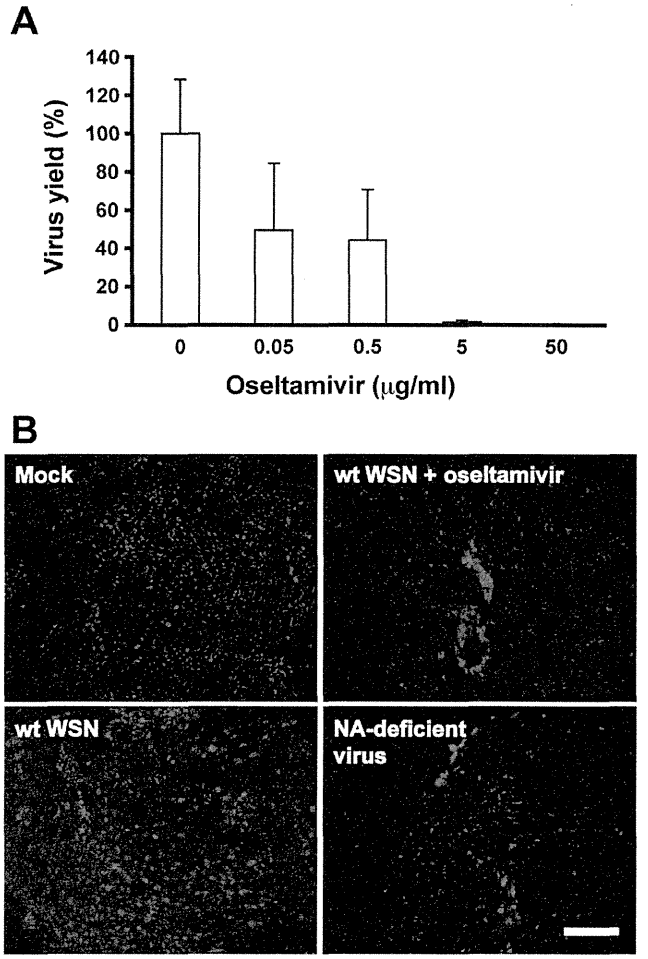

Figure 1. Influenza viruses can spread independent of the NA activity. (A) MDCK cells were infected with influenza virus A/WSN/33 at a multiplicity of infection (MOI) of 0.001 PFU per cell. At 48 hours post infection (hpi), culture supernatant was collected, and then its virus titer was determined by plaque assays. Each result was represented by a value relative to that in the absence of the drug. Error bars indicate standard deviation (s.d.) from 3 independent experiments. (B) Confluent MDCK cells were infected by wild-type influenza virus A/WSN/33 or NA-deficient influenza virus at MOI of 0.0001 in the presence or absence of 50 μg/ml oseltamivir phosphate. NA-deficient influenza virus was generated by reverse genetics as previously described [29]. After incubation at 37°C for 36 hours, immunofluorescence analyses were performed using anti-nucleoprotein (NP) polyclonal antibody and anti-rabbit IgG antibody conjugated to Alexa Fluor 568 (Invitrogen). Scale bar, 100 μm.
doi:10.1371/journal.pone.0028178.g001

number of single fluorescent foci caused by initial infection markedly expanded and formed cell clusters consisting of 5–10 infected cells in an MDCK cell monolayer (Figures 1B and S1), suggesting influenza virus can spread to some extent in the presence of oseltamivir. To verify that NA is not involved in this spreading, we generated an NA-deficient influenza virus by a reverse genetics method as described previously [29,30]. The NA-deficient influenza virus contains a mutated NA segment, in which the NA coding region including a sialidase catalytic domain was replaced with the *enhanced green fluorescent protein (EGFP)* gene [29]. By this replacement, the NA activity is eliminated from the recombinant influenza virus, and *EGFP* can be utilized as a marker for viral infections. Immunofluorescence analyses demonstrated that the NA-deficient influenza virus also forms infected cell

clusters similarly to those formed by wild-type influenza virus in the presence of oseltamivir (Figure 1B). The fluorescence pattern of NP overlapped with the localization of GFP derived from the *EGFP* gene of the NA-deficient influenza virus (Figure S2). Thus, NA-deficient influenza virus can be used to investigate the NA-independent infection pathway of influenza virus.

Next, we performed live cell imaging analyses to directly observe the infection time course of the NA-deficient influenza virus. The GFP fluorescence derived from the NA-deficient influenza virus first appeared in a single cell on an MDCK cell monolayer at 24 hours post infection. The virus started to spread from an infected cell to adjacent cells in 5–6 hours after the first appearance of a GFP-positive cell (Figure 2 and Video S1). The spreading rate was clearly faster than the rate of cell divisions. The mean doubling time of uninfected MDCK cells was 20–24 hours under the condition employed here, and it is expected that the proliferation speed would be much slowly because infected MDCK cells were maintained in the serum-free medium and formed cell monolayer at the high cell density. These suggest that NA-deficient influenza viruses may infect adjacent cells through the cell-to-cell transmission mechanism without apparent production of *cell-free* virions.

Cell-to-cell transmission pathway of influenza viruses is less sensitive to neutralizing antibody

The cell-to-cell virus transmission pathway could be interpreted as one of viral evolving strategies to avoid neutralizing antibody responses [2,31,32]. Therefore, we examined the effect of neutralizing antibody on NA-deficient influenza virus. A polyclonal antibody with the neutralizing activity against influenza virus particles inhibited infection of *cell-free* viruses to less than 50% at the concentration of 0.03%, although the cell cluster formation was observed at the concentration less than 0.01%. On the other hand, the NA-independent transmission of the NA-deficient influenza virus was blocked only when neutralizing antibody was present at the concentration of 0.3% (Figure 3). These results indicated that the NA-independent transmission of influenza viruses is less sensitive to the neutralizing antibody.

NA-independent transmission of influenza virus is HA-dependent

Next, to investigate the mechanism of NA-independent transmission of influenza virus, we examined whether HA is involved in this transmission. In the absence of the NA activity, virus spreading from an infected cell to adjacent cells was dramatically suppressed by omission of trypsin, essential for maturation of HA, from the experimental condition (Figure 4A). The GFP fluorescence derived from NA-deficient influenza virus appeared in a single cell at 24 hours post infection. However, this virus did not spread, but rather disappeared during subsequent 24 hours (Video S2). These observations indicate that the NA-independent cell-to-cell transmission of influenza virus is dependent on HA maturation mediated by trypsin, as is the case for the general *cell-free* transmission of this virus.

To clarify whether virus particles or viral RNP complexes are transmitted to adjacent cells, we examined the effect of amantadine on the cell-to-cell transmission of influenza virus. Amantadine inhibits the early step of uncoating of influenza virus RNP from virion in endosomes [33,34]. For this study, other influenza virus strain, influenza virus A/Udorn/72, was used instead of influenza virus A/WSN/33 because influenza virus A/WSN/33 is highly resistant to amantadine [35]. We confirmed that influenza virus A/Udorn/72 is sensitive to oseltamivir (Figure S3) and could also spread via cell-to-cell transmission independent of the NA activity as did for influenza virus A/WSN/33 (Figures 1B and 4B). In the case of a single administration of amantadine, fluorescent foci derived from infected cells scattered, and the number of single foci was greatly decreased compared

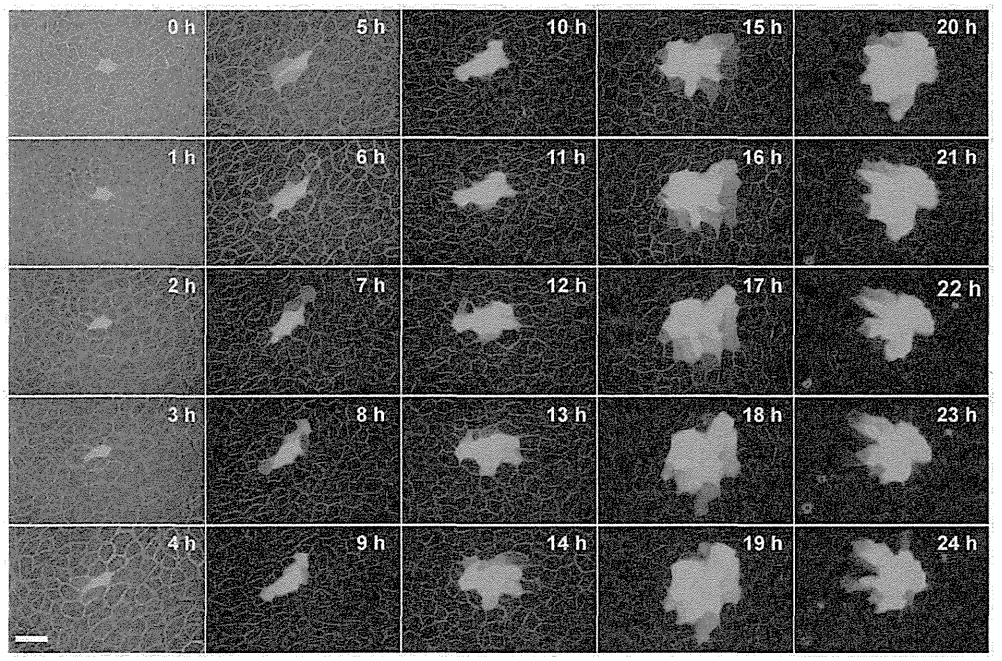

Figure 2. NA-deficient influenza virus spreads through cell-to-cell transmission. Confluent MDCK cells were infected with the NA-deficient influenza virus at MOI of 0.0001. After incubation at 37°C for 24 hours, a single GFP-positive cell, in which the recombinant virus replicated, was found at 1 hour after starting monitoring, and then this cell and its neighborhood were traced during the period from 24 hpi to 48 hpi at interval of 1 hour. Scale bar, 50 μm.
doi:10.1371/journal.pone.0028178.g002

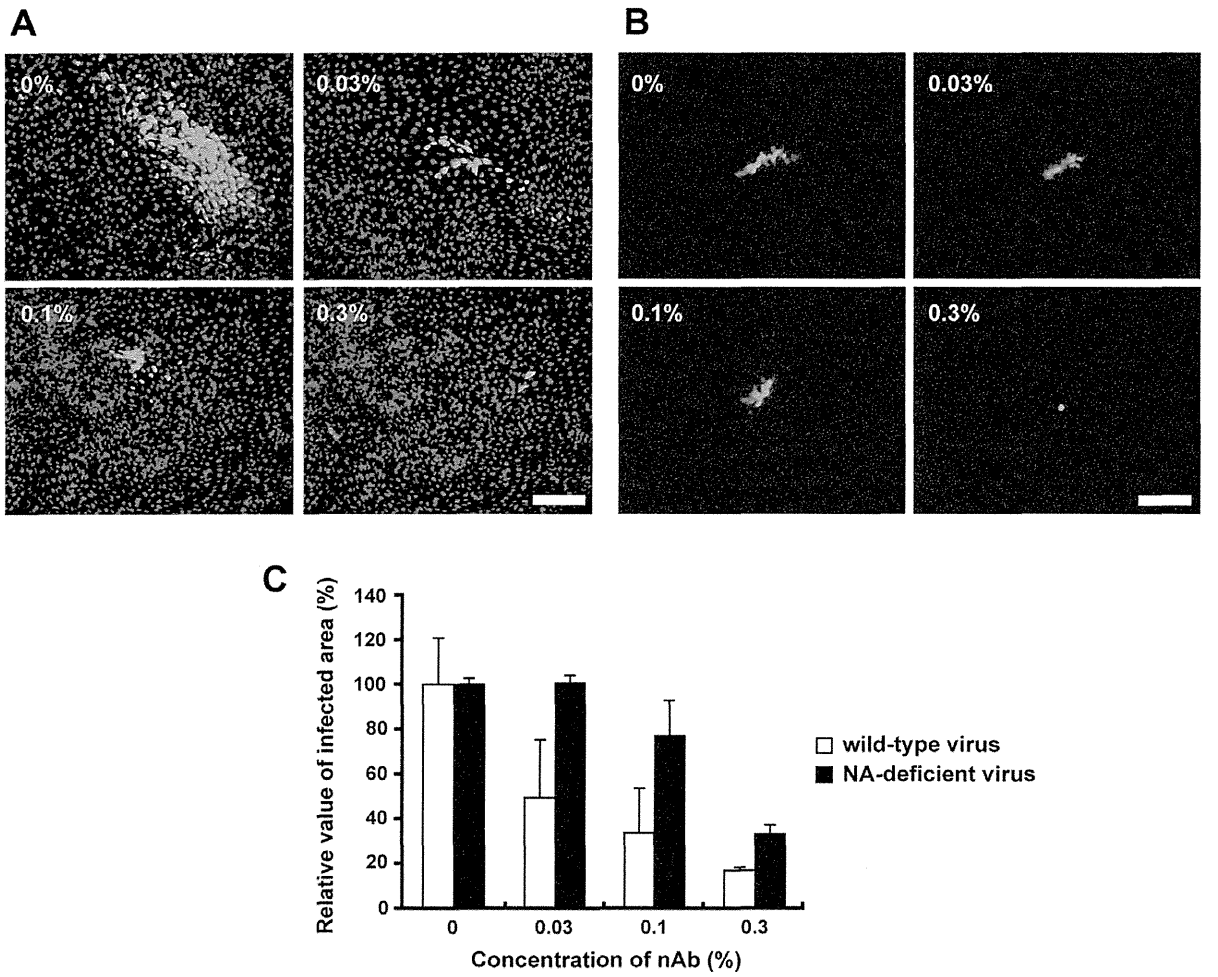

Figure 3. The cell-to-cell transmission of the NA-deficient influenza virus is less sensitive to the neutralizing antibody. (A) Infection of the wild-type and (B) NA-deficient influenza virus were performed in the presence or absence of antiserum containing neutralizing antibodies. Immunofluorescence analyses were performed with cells infected with wild-type influenza virus at 18 hpi using anti-NP antibody and anti-rabbit IgG antibody conjugated to Alexa Fluor 488 (Invitrogen). GFP fluorescence derived from the recombinant virus was observed at 36 hpi. Scale bar, 100 μm. (C) The level of viral spreading was indicated in the graph by measuring NP and GFP derived from wild-type and NA-deficient virus, respectively. Five different microscope fields were taken randomly, and then the intensity of green color was analyzed with ImageJ NIH image processing software. Each result was represented by a value relative to that in the absence of neutralizing antibodies. Error bars indicate s.d. from 3 independent experiments.
doi:10.1371/journal.pone.0028178.g003

with that in the absence of the drugs. In contrast, a single administration of oseltamivir, fluorescent foci formed some clusters and expanded in a time-dependent manner (Figure 4B). This dissimilarity of inhibitory manner was caused by the difference of the sites of action between amantadine and oseltamivir. Amantadine inhibits the replication of influenza A virus by preventing the translocation of vRNP complexes from endosomes to the cytoplasm, whereas oseltamivir has no effects on viral replication itself but inhibits the release of *cell-free* virions from infected host cells. We investigated the inhibitory effect of amantadine on the cell-to-cell transmission of influenza viruses. The formation of infected cell clusters was observed with co-administration of amantadine and oseltamivir, as well as with a single administration of oseltamivir (Figure 4B). However, the quantitative analysis revealed that the size of infected cell clusters with the co-administration were decreased as compared to that with oseltamivir alone (Figure 4C). These observations indicated that the NA activity-independent cell-to-cell transmission of influenza virus was susceptible to the inhibitory effect of amantadine, suggesting that the cell-to-cell transmission undergoes through endocytosis but vRNP complex itself is not incorporated in the infected cells by adjacent cells.

Cell-to-cell transmission occurs on the apical cell membrane

The virus transmission undergoes from infected to uninfected cells through either basolateral [36–38] or apical [39–42] sides. In the case of influenza virus, *cell-free* progeny virions are released only from the apical surface of polarized epithelial cells [43]. This releasing polarity is achieved by directed transport of viral membrane proteins to the apical plasma membrane [44]. Indeed, that HA and NA glycoproteins are associated with lipid rafts, and the raft association has been implicated in apical transport [45,46].

To determine whether or not the cell-to-cell transmission of the NA-deficient influenza virus occurs on the apical surface, we performed transwell assays in the presence of the neutralizing antibody to influenza A viruses. The neutralizing antibody was added to infected MDCK cell monolayer from apical or

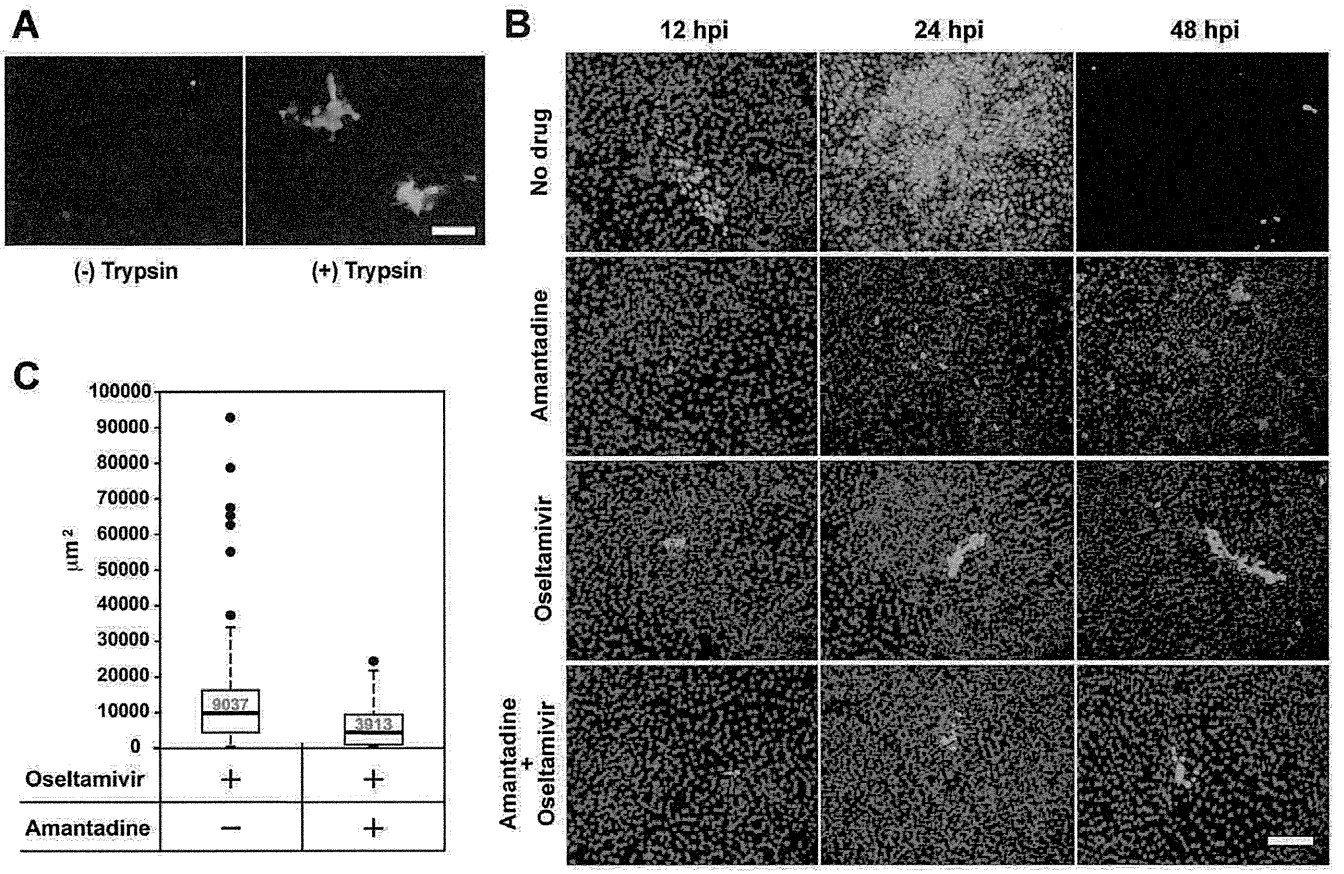

Figure 4. The cell-to-cell transmission of the NA-deficient influenza virus requires functional HA. (A) Confluent MDCK cells were infected with the NA-deficient influenza virus at MOI of 0.0001 in the presence or absence of 1 μg/ml trypsin. GFP fluorescence derived from the recombinant virus was observed at 36 hpi. Scale bar, 100 μm. (B) MDCK cells were infected with influenza virus A/Udorn/72 at moi of 0.0001 in the presence or absence of 50 μM amantadine or 50 μg/ml oseltamivir phosphate. Amantadine at the concentration of 50 μM almost completely inhibited the production of progeny virions (data not shown). After incubation for 12, 24, and 48 h, immunofluorescence analyses were performed using anti-NP antibody and anti-rabbit IgG antibody conjugated to Alexa Fluor 488 (Invitrogen). Viral NP and nuclear DAPI staining are shown in green and blue, respectively. Scale bar, 100 μm. (C) Median sizes of clusters were shown as box plots summarizing sizes of 60 individual infectious foci formed in the presence of oseltamivir alone, or both oseltamivir and amantadine. Immunofluorescence analyses were performed as described in (B) at 24 hpi. Boxes enclose the lower and upper quartiles; thick horizontal lines represent the median; dashed lines indicate the extreme values; and black dots are outliers of individual infectious foci. The size of infectious foci was measured with AxioVision Release 4.7.2 imaging software (Carl Zeiss). Median sizes shown in red letters were clearly different from each other ($p<0.01$).
doi:10.1371/journal.pone.0028178.g004

basolateral side, and the inhibitory effect on the spread of GFP fluorescence derived from the recombinant virus was examined. Addition of high concentrations of the neutralizing antibody from the apical side blocked the cell-to-cell transmission of the NA-deficient influenza virus, whereas the addition from the basolateral side had no effect (Figure 5). These observations indicated that the polarity in the influenza virus budding in the cell-to-cell transmission pathway is apical.

Influenza viruses can not re-infect previously infected cells

Previous report showed that influenza viruses were refractory to superinfection with a second cell-free virus [23]. In the case of the cell-to-cell transmission of influenza virus in the presence of oseltamivir, it is possible that a progeny virion is temporarily bridged by HA between an infected cell and adjacent uninfected cells, since viruses can not be released from infected cell surface due to the inhibition of the NA activity by oseltamivir. The cell-associated progeny virion may have an opportunity to re-infect the previously infected cell, compared to a cell-free progeny virion in the general spreading. Thus, we examined whether influenza viruses can infect the cell which had already been infected, using *ts*53 mutant and wild-type influenza virus A/WSN/33. *ts*53 virus has a substitution mutation from U to C at the nucleotide position of 701 in the PA gene. This substitution introduces an amino acid change from wild-type Leu 226 to Pro 226 and gives a defect in the viral genome replication process [47,48]. At first, cells were infected with *ts*53 virus at moi of 10, and after incubation for 0, 2, 4, 6, and 8 hours, cells were superinfected with wild-type virus at moi of 10. The amount of segment 3 viral RNA (vRNA) encoding PA was determined quantitatively by RT-PCR. Then, using a mutated primer for PCR, we could introduce a *Stu* I site only in the PCR products derived from the wild-type sequence (Figure 6A). Thus, DNA fragments amplified from the wild-type and *ts*53 could be distinguished by *Stu* I digestion. The digested DNA fragments containing 220 and 199 base pairs derived from *ts*53 and wild-type, respectively, were separated through PAGE. After 6 hours or later post infection, re-infection with the second challenging virus hardly occurs in the absence of oseltamivir. However, in the presence of oseltamivir, appearance of wild-type fragment suggests that the re-infection had occurred (Figure 6B). The result indicates

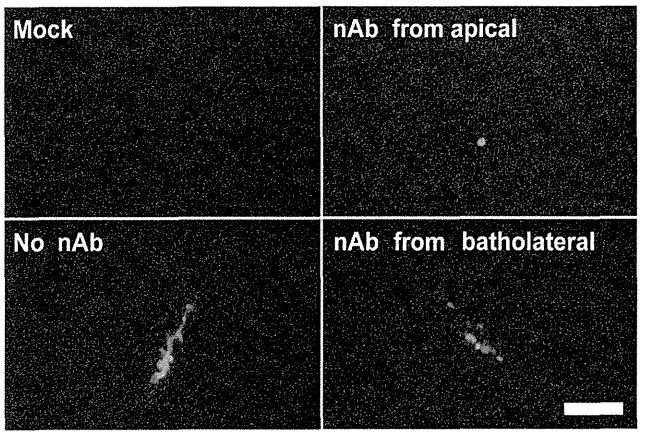

Figure 5. The cell-to-cell transmission of the NA-deficient influenza virus occurs the apical cell surface. Confluent MDCK cells were prepared in transwell inserts and infected with the NA-deficient influenza virus at MOI of 0.0001 in the presence or absence of 0.3% (v/v) antiserum containing neutralizing antibodies (nAb) to influenza A virus. After virus adsorption, the antiserum was added from apical or basolateral side. GFP fluorescence derived from the recombinant virus was observed at 36 hpi. The antiserum added from the apical side could markedly block the cell-to-cell transmission of the NA-deficient influenza virus, whereas the antiserum added from the basolateral side could not. Scale bar, 100 μm.
doi:10.1371/journal.pone.0028178.g005

that progeny virus particles remain on the surface of infected cell even after budding, and can infect the cell previously infected, as well as uninfected cells adjacent to the infected cell, when oseltamivir is present.

Discussion

With the except for the virus which spreads through the cell-cell fusion transmission, virus infection is initiated by the binding of *cell-free* virions to their host cells. Recently, the virus transmission mechanism from an infected cell to adjacent cells without virus diffusion into the extracellular environment is highlighted from the aspect of its significance in virus spreading in the presence of antibodies [1,2]. This antibody-insensitive pathway is often called cell-to-cell transmission [2]. The cell-to-cell transmission may be categorized into two pathways, *i.e.*, transmission of *cell-free* virions to adjacent uninfected cells, and transmission of progeny virions associated on the surface of an infected cell even after budding through narrow synaptic space between an infected cell and adjacent uninfected cells. As an example of the former mechanism, *cell-free* vaccinia virus particles associated with the filopodium of an infected cell are repelled toward neighboring uninfected cells by inducing the formation of actin filament [3]. Several cases have been reported for the latter mechanism: Immunotropic viruses including retroviruses utilize the immunological synapses [4–7]. Immune cells are not constitutively polarized, but contain the machinery that directs their secretory apparatus towards a cell that is involved in an immunological synapse. This machinery can be subverted by retroviruses containing human immunodeficiency virus (HIV). An HIV-infected cell can polarize viral budding towards a target cell expressing receptor through a structure called a virological synapse. Virions bud from an infected cell into a synaptic cleft, from which they fuse with the target-cell plasma membrane [49–52]. The progeny virions of HCV are trapped between infected and uninfected cell membranes at the tight junction. Using Claudin-1 known as a component of the tight junction and one of the entry factors of HCV [8], virions fuse with and penetrate uninfected target cells [31]. Therefore, HCV may acquire the ability to spread within polarized liver epithelium. Thus, the cell-to-cell transmission certainly plays significant roles for the dissemination of several enveloped viruses. However, the cell-to-cell transmission of influenza virus has not been discussed well. Here, we have shown that influenza virus spreads by forming infected cell clusters even in the presence of an NA inhibitor. Live cell imaging clearly showed that influenza virus lacking the NA activity spreads from an infected cell to adjacent cells through the cell-to-cell transmission mechanism (Figure 2). This was also the case for wild-type influenza virus during early phases of infection (Figure 4B). In the cell-to-cell transmission of influenza virus, progeny virions could remain associated with the surface of infected cell even after budding, and then these progeny virions can be passed on to adjacent uninfected cells.

We showed that the cell-to-cell transmission of the NA-deficient influenza virus depends on functional HA. The viral spreading was dramatically suppressed without HA activation by trypsin treatment (Figure 4A). Moreover, the cell-to-cell transmission was also blocked by amantadine, which inhibits the acidification of endosomes required for uncoating of influenza virus particles in endosomes [33,34]. These findings indicate that functional HA and endosome acidification by M2 ion channel are required for the cell-to-cell influenza virus transmission, thereby allowing viruses to enter the adjacent cells through the endocytotic pathway (Figure 4).

Our findings showed that the NA-deficient influenza virus is not diffused into the extracellular environment. The viral spreading in the absence of oseltamivir appears to be much faster compared to the viral spreading in the presence of the drug, suggesting that NA could be involved in determination of spreading speed (Figure 4B). The NA activity prevented progeny virions from entering cells which virus came from (Figure 6), implying that progeny virus particles should be transmitted to adjacent uninfected cells. The cell-to-cell transmission started in early phase of infection, and the virus spread through diffusion of *cell-free* viruses (Figure 4B). Indeed, it was reported that the cell-to-cell transmission is a rapid spreading pathway in the case of vaccinia virus [3]. Vaccinia virus induces a blocking mechanism of superinfection and thereby infects to adjacent uninfected cells efficiently. In early phases of vaccinia virus infection, viral proteins A33 and A36 are expressed at the infected cell surface. Once *cell-free* virus particles contact the filopodium, the A33/A36 complex induces the formation of actin filament, which causes this superinfected virion to be repelled toward uninfected cells [3]. Influenza viruses can re-infect the cells previously infected in the presence of oseltamivir (Figure 6), suggesting that a progeny virion may be bridged by HA between infected and adjacent uninfected cells temporarily. Thus, in the case of the cell-to-cell transmission of influenza virus, we propose that progeny virions associated with the surface of infected cells even after budding are directed to adjacent uninfected cells. The cell-to-cell transmission mechanism of influenza virus is distinctly different from that of vaccinia virus in the infecting virus status: Infected cell-associated virions and *cell-free* virions are involved in the cell-to-cell transmission of influenza virus and vaccinia virus, respectively. The strategy for influenza virus appears to be similar to that for HCV. HCV progeny virions budded from an infected cell are trapped between infected and uninfected adjacent cell membranes at the tight junction. HCV virions then, enter into adjacent cells through endocytosis and low pH-dependent membrane fusion using Claudin-1 [8]. The cell-to-cell transmission of influenza virus also required functional HA and endosome acidification by M2 ion channel. However, it has not been reported that HCV has a gene encoding a receptor destroying

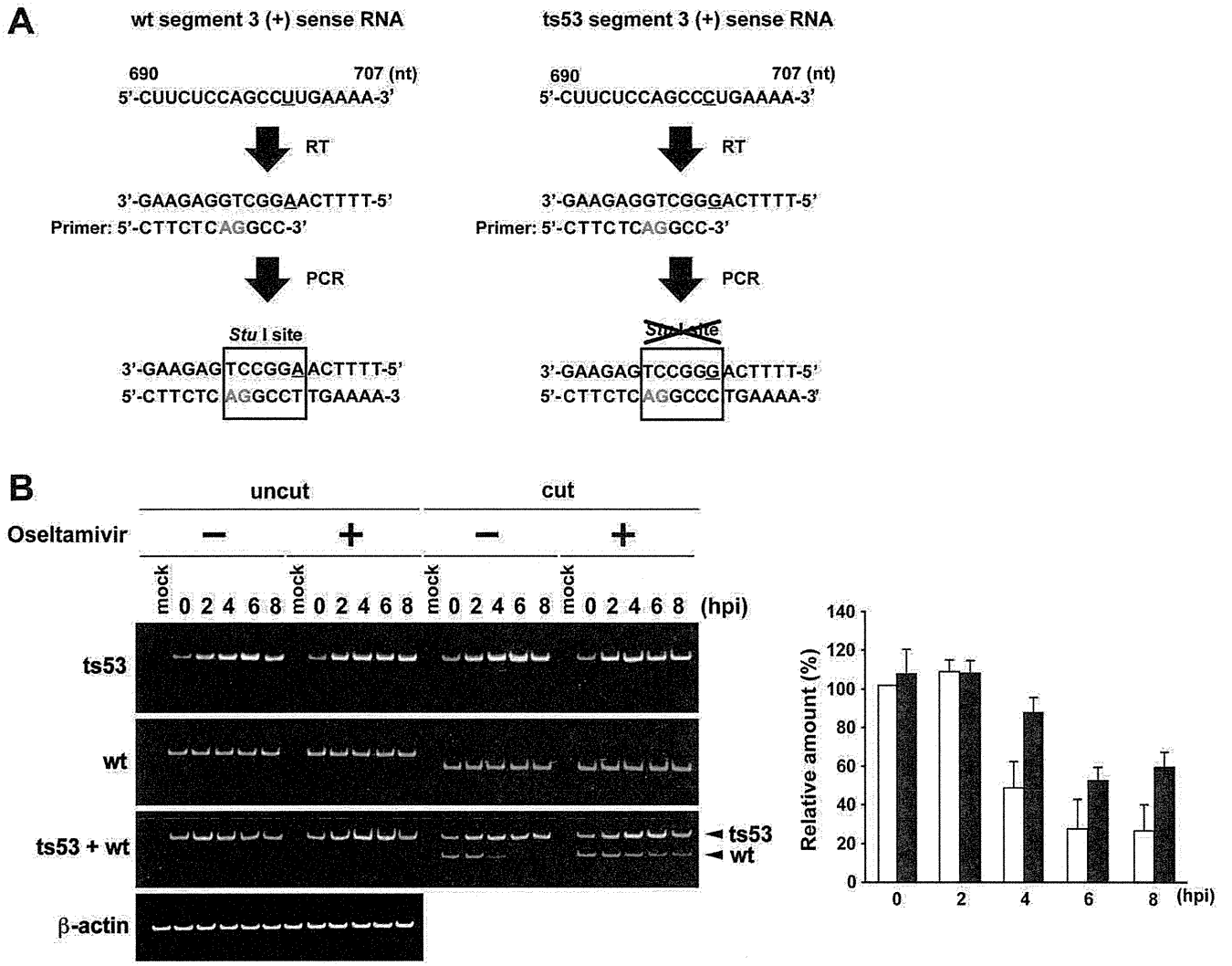

Figure 6. Influenza viruses can not re-infect previously infected cells. (A) A method for determination of the amount of segment 3 genome derived from *ts*53 and wild-type. Total RNA was reverse-transcribed with the primer PA-895-rev, which is complementary to the segment 3 positive-sense RNA. The cDNA was amplified by PCR using primers, PA-895-rev and PA-695-cut partially corresponding to segment 3 positive sense RNA between the nucleotide sequence positions 678 to 700 except for 696 and 697, which are shown in red letters. Since segment 3 of *ts*53 has a substitution mutation from U to C at the nucleotide position of 701, the PCR product derived from wild-type could be digested by *Stu* I but not that from *ts*53. Then, PCR products were digested with *Stu* I and separated through 8% PAGE. (B) Detection of the genome of the segment 3 derived from *ts*53 or wild-type. At 3 hours post superinfection of wild-type virus, total RNA was extracted, and semi-quantitative RT-PCR was performed. Subsequently, the amplified DNA products were digested with *Stu* I and separated through 8% PAGE. Large and small fragments derived from *ts*53 and wild-type viruses were 220 and 199 base pairs, respectively. The relative amount of wild-type segment 3 to that at 0 hour in the absence of oseltamivir phosphate was shown in the graph. Error bars indicate S.D. from 3 independent experiments. White bar, in the absence of oseltamivir phosphate; black bar, in the presence of oseltamivir phosphate.
doi:10.1371/journal.pone.0028178.g006

enzyme similar to NA of influenza virus. We speculated that HCV progeny particles are bridged between infected and adjacent uninfected cells temporarily like influenza virus in the presence of oseltamivir. Progeny influenza virus particles could be transmitted to adjacent uninfected cells efficiently in the presence of the NA activity, suggesting that the cell-to-cell transmission of influenza virus is more strategic than that of HCV.

Our findings raise an interesting question as to what is the biological significance of cell-to-cell transmission for influenza virus infection *in vivo*. Until now, it had been believed that influenza virus was released from infected cells as *cell-free* virions and then spread from cell to cell as well as from organism to organism. The transmission mode by *cell-free* virions undergoes the extremely high-speed of its diffusion and causes epidemic or pandemic infection. The tropism in an infected animal body is generally restricted to respiratory tract or lung and its periphery, and the requirement of a trypsin-like protease has been generally described for the reason of the restriction. It is possible that the cell-to-cell transmission mode may play a significant role for the virus spreading inside of organism, although *cell-free* influenza virions are causative of high-speed spreading. At the least, the limited but distinct level of infection followed by replication could provide some opportunity to generate influenza virus variants. It is an open question whether the cell-to-cell transmission mode is involved in the pathogenesis caused by influenza virus infection *in vivo*.

The existence of cell-to-cell transmission pathway gives a caution when NA inhibitors are used, because NA inhibitors may not be sufficient to completely block the spread of influenza

virus in local microenvironments. Since this cell-to-cell transmission pathway exists, development of antiviral therapeutic strategies in addition to NA inhibitors is highly recommended.

Materials and Methods

Cells and viruses

Madin-Darby canine kidney (MDCK) cells were kindly gifted by A. Ishihama (Hosei University), and maintained in minimal essential medium (MEM) (Nissui) containing 10% fetal bovine serum. Human embryonic kidney 293T cells were kindly gifted by Y. Kawaoka (University of Tokyo), and maintained in Dulbecco modified Eagle medium (DMEM) (Nissui) supplemented with 10% fetal bovine serum. Influenza virus A/Udorn/72 was grown in allantoic sacs of 11 day-old embryonated eggs (MIYAKE HATCHERY). Wild-type influenza virus A/WSN/33 and *ts*53 mutant were used after single-plaque isolation. MDCK cells were infected with influenza virus A/WSN/33 or *ts*53 at a multiplicity of infection (MOI) of 0.1 PFU/cell, and incubated at 37°C and 34°C, respectively. After incubation for 24 h, the culture fluid was harvested and centrifuged at 1,700× *g* for 10 min. The virus suspension was stored at −80°C until use.

Antibodies

The production of rabbit polyclonal anti-NP antibody was described previously [53], and this antibody was used as a primary antibody for indirect immunofluorescence assay. A goat anti-rabbit IgG antibody conjugated to Alexa Fluor 488 or Alexa Fluor 568 was purchased from Invitrogen and used as a secondary antibody for indirect immunofluorescence assay. A polyclonal antibody against influenza A virus was obtained from 2-month-old female rabbit immunized with 250 μg of purified virions of influenza virus strain A/Puerto Rico/8/34 [54]. The generation of antibodies was boosted three times and used as neutralizing antibodies to block the influenza virus infection.

Determination of the inhibition effect of oseltamivir on virus production

MDCK cells were infected with influenza virus A/WSN/33 at a multiplicity of infection (MOI) of 0.001 PFU per cell. After virus adsorption at 37°C for 1 hour, the cells were washed with serum-free MEM and incubated at 37°C with maintenance medium (MEM containing vitamins and 0.1% BSA) containing oseltamivir. At 48 hours post infection (hpi), culture supernatant was collected, and then its viral titer was determined by plaque assays.

Generation of neuraminidase (NA)-deficient viruses

An NA-deficient influenza virus possessing the terminal sequences of NA segment but lacking the NA coding region, which was replaced with *enhanced green fluorescent protein (EGFP)* gene, was generated by reverse genetics as described previously [29,30]. For reverse genetics, we used plasmids containing cDNAs of the influenza virus A/WSN/33 viral genome under the control of the human RNA polymerase I promoter (referred to as Pol I plasmids). Briefly, 293T cells were transfected with seven Pol I plasmids for production of all vRNA segments of influenza virus A/WSN/33 and one for the mutant NA vRNA segment containing *EGFP* ORF, together with protein expression vectors for PB2, PB1, PA, and NP controlled by the chicken β-actin promoter (pCAGGS). TransIT-293 (Mirus) was used for transfection. At 24 hours post transfection, recombinant viruses were harvested from the cell surface using bacterial NA derived from *Clostridium perfringens* (sigma). MDCK cells were infected with harvested recombinant viruses treated with *N*-tosyl-L-phenylalanine chloromethyl ketone (TPCK)-trypsin (1 μg/ml). After confirmation of GFP fluorescence derived from amplified recombinant virus genomes at 48 hours after infection, the recombinant viruses on the cell surface were collected using bacterial NA. The viral titer of recombinant viruses was determined by counting the number of infected foci using a fluorescence microscopy (Carl Zeiss).

Indirect immunofluorescence assay

Cells on coverslips were fixed with 4% paraformaldehyde in phosphate-buffered saline (PBS) for 10 min and permeabilized with 0.2% NP-40 in PBS. The coverslips were soaked in 1% bovine serum albumin in PBS, and then incubated at room temperature for 1 hour with a primary antibody. After being washed twice with PBS, the coverslips were incubated at room temperature for 1 hour with a secondary antibody. The coverslips were then incubated at room temperature for 5 min with 3 μM 4′,6′-diamidino-2-phenylindole (DAPI) and finally mounted on glass plates, and cells were observed under the fluorescence microscope.

Live cell imaging analyses

Living cells were analyzed using BioStation ID system (GE Healthcare). Confluent MDCK cells were infected with the NA-deficient influenza virus at the multiplicity of infection (MOI) of 0.0001 in the presence or absence of 1 μg/ml TPCK-trypsin. At 24 hours post infection, culture dishes containing infected cells were set into the chamber of BioStaion ID system, which was maintained at 37°C under 5% CO_2 and 95% humidity. Then, images were acquired during next 24 hours at interval with 1 hour. The excitation wavelength was controlled by a manual filter wheel equipped with filters suitable for enhanced green fluorescence protein (EGFP).

Transwell assay

Confluent MDCK cell monolayer was prepared on transwell inserts (BD Falcon, pore size 0.4 μm) and infected with the NA-deficient influenza virus at MOI of 0.0001. After virus adsorption at 37°C for 1 hour, the cell monolayer was washed with serum-free MEM, and maintenance medium was added into both sides within the transwells. The neutralizing antibody to influenza A virus was added into the inside or the outside of transwell inserts with the maintenance medium. Subsequently, cells were incubated at 37°C for 36 hours followed by analyses using the fluorescence microscopy.

RT-PCR

*ts*53 virus has a substitution mutation from U to C at the nucleotide position of 701 in the *PA* gene. This substitution introduces an amino acid change from wild-type Leu 226 to Pro 226 and gives a defect in the viral genome replication process [48]. However, under the permissive temperature, the level of viral genome replication is no difference between wild-type and *ts*53 [47]. To discriminate the genome of wild-type and that of *ts*53, total RNA was reverse-transcribed by reverse transcriptase (TOYOBO) with PA-895-rev (5′-TTAATTTTAAGGCATC-CATCAGCAGG-3′), which is complementary to the segment 3 positive sense RNA. The cDNA was amplified by PCR using primers, PA-895-rev and PA-695-cut (5′-TCTCCCGCCA-AACTTCTCAGGCC-3′) partially corresponding to segment 3 positive sense RNA between nucleotide sequence positions 678 to 700 except for nucleotide positions 696 and 697. Since segment 3 of *ts*53 has a substitution mutation from U to C at the nucleotide position of 701, the PCR product derived from wild-type was digested by *Stu* I but not that from *ts*53. After PCR reactions, PCR

products were digested with *Stu* I and separated through PAGE. Large and small fragments derived from *ts*53 and wild-type viruses were 220 and 199 base pairs, respectively. DNA was stained with GelRed (BIOTIUM) and visualized by UV illumination.

Supporting Information

Figure S1 Formation of cell cluster caused by initial infection. MDCK cells were infected with influenza virus A/WSN/33 at moi of 0.0003 in the presence or absence of 50 μg/ml oseltamivir phosphate. After incubation for 8 and 24 h, immunofluorescence analyses were performed using anti-NP antibody and anti-rabbit IgG antibody conjugated to Alexa Fluor 488 (Invitrogen). Nuclear DAPI and viral NP staining patterns are shown in blue and green, respectively. Enlarged views are shown in red borders. Scale bar, 100 μm.
(TIF)

Figure S2 The expression of GFP derived from NA-deficient influenza virus overlapped with the localization of NP. MDCK cells were infected with NA-deficient influenza viruses at MOI of 0.0001. After incubation at 37°C for 48 hours, immunofluorescence analyses were performed using anti-NP antibody. Scale bar, 100 μm.
(TIF)

Figure S3 Influenza virus A/Udorn/72 was sensitive to oseltamivir. MDCK cells were infected with influenza virus A/Udorn/72 at a MOI of 0.001 PFU per cell. At 36 hpi, the culture supernatant was collected, and then its virus titer was determined by plaque assays. Each result was represented by a value relative to that in the absence of the drug. Error bars indicate s.d. from 3 independent experiments.
(TIF)

Video S1 NA-deficient influenza virus spreads through cell-to-cell transmission. Confluent MDCK cells were infected with NA-deficient influenza virus at MOI of 0.0001 in the presence of trypsin. After incubation at 37°C for 24 hours, a single GFP-positive cell and its vicinity were traced it during the period from 24 hpi to 48 hpi at interval of 1 hour. Live cell imaging data analyses was performed by Biostation ID (GE healthcare). Scale bar, 50 μm.
(MOV)

Video S2 NA-deficient influenza virus does not spread in the absence of trypsin. Confluent MDCK cells were infected with the NA-deficient influenza virus at MOI of 0.0001 in the absence of trypsin. After incubation at 37°C for 24 hours, a single GFP-positive cell was detected, and then this cell and neighborhood cells was traced during the period from 24 hpi to 48 hpi at interval of 1 hour. Live cell imaging data analyses were performed by Biostation ID (GE healthcare). Scale bar, 50 μm.
(MOV)

Acknowledgments

We thank A. Ishihama (Hosei University) for MDCK cells, Y. Kawaoka (University of Tokyo) for 293T cells. We also thank K. Ho for his careful proofreading of the manuscript. We are grateful to A. Kawaguchi (Kitasato University and University of Tsukuba) for his valuable discussion during the course of this work.

Author Contributions

Conceived and designed the experiments: KM TH KN. Performed the experiments: KM TH. Analyzed the data: KM TH KN. Contributed reagents/materials/analysis tools: TH. Wrote the paper: KM TH KN.

References

1. Sattentau Q (2008) Avoiding the void: cell-to-cell spread of human viruses. Nat Rev Microbiol 6: 815–826.
2. Mothes W, Sherer NM, Jin J, Zhong P (2010) Virus Cell-to-Cell Transmission. J Virol 84: 8360–8368.
3. Doceul V, Hollinshead M, van der Linden L, Smith GL (2010) Repulsion of superinfecting virions: a mechanism for rapid virus spread. Science 327: 873–876.
4. Igakura T, Stinchcombe JC, Goon PK, Taylor GP, Weber JN, et al. (2003) Spread of HTLV-I between lymphocytes by virus-induced polarization of the cytoskeleton. Science 299: 1713–1716.
5. Dustin M (2003) Viral spread through protoplasmic kiss. Nat Cell Biol 5: 271–272.
6. Hübner W, McNerney GP, Chen P, Dale BM, Gordon RE, et al. (2009) Quantitative 3D video microscopy of HIV transfer across T cell virological synapses. Science 323: 1743–1747.
7. Pais-Correia AM, Sachse M, Guadagnini S, Robbiati V, Lasserre R, et al. (2010) Biofilm-like extracellular viral assemblies mediate HTLV-1 cell-to-cell transmission at virological synapses. Nat Med 16: 83–89.
8. Evans MJ, von Hahn T, Tscherne DM, Syder AJ, Panis M, et al. (2007) Claudin-1 is a hepatitis C virus co-receptor required for a late step in entry. Nature 446: 801–805.
9. Ploss A, Evans MJ, Gaysinskaya VA, Panis M, You H, et al. (2009) Human occludin is a hepatitis C virus entry factor required for infection of mouse cells. Nature 457: 882–886.
10. Barton ES, Forrest JC, Connolly JL, Chappell JD, Liu Y, et al. (2001) Junction adhesion molecule is a receptor for reovirus. Cell 104: 441–451.
11. Balfe P, McKeating JA (2009) The complexities of hepatitis C virus entry. J Hepatol 51: 609–611.
12. Wiley DC, Skehel JJ (1987) The structure and function of the hemagglutinin membrane glycoprotein of influenza virus. Annu Rev Biochem 56: 365–394.
13. Suzuki Y, Ito T, Suzuki T, Holland RE, Chambers TM, et al. (2000) Sialic acid species as a determinant of the host range of influenza A viruses. J Virol 74: 11825–11831.
14. Skehel JJ, Bayley PM, Brown EB, Martin SR, Waterfield MD, et al. (1982) Changes in the conformation of influenza virus hemagglutinin at the pH optimum of virus-mediatedmozawa T, membrane fusion. P Natl Acad Sci Usa 79: 968–972.
15. Skehel JJ, Waterfield MD (1975) Studies on the primary structure of the influenza virus hemagglutinin. P Natl Acad Sci Usa 72: 93–97.
16. Sato M, Yoshida S, Iida K, Tomozawa T, Kido H, et al. (2003) A novel influenza A virus activating enzyme from porcine lung: purification and characterization. Biol Chem 384: 219–227.
17. Lazarowitz SG, Choppin PW (1975) Enhancement of the infectivity of influenza A and B viruses by proteolytic cleavage of the hemagglutinin polypeptide. Virology 68: 440–454.
18. Klenk HD, Rott R, Orlich M, Blödorn J (1975) Activation of influenza A viruses by trypsin treatment. Virology 68: 426–439.
19. Kido H, Yokogoshi Y, Sakai K, Tashiro M, Kishino Y, et al. (1992) Isolation and characterization of a novel trypsin-like protease found in rat bronchiolar epithelial Clara cells. A possible activator of the viral fusion glycoprotein. J Biol Chem 267: 13573–13579.
20. Bullough PA, Hughson FM, Skehel JJ, Wiley DC (1994) Structure of influenza haemagglutinin at the pH of membrane fusion. Nature 371: 37–43.
21. Tamm LK, Han X, Li Y, Lai AL (2002) Structure and function of membrane fusion peptides. Biopolymers 66: 249–260.
22. Air GM, Laver WG (1989) The neuraminidase of influenza virus. Proteins 6: 341–356.
23. Huang IC, Li W, Sui J, Marasco W, Choe H, et al. (2008) Influenza A virus neuraminidase limits viral superinfection. J Virol 82: 4834–4843.
24. Palese P, Tobita K, Ueda M, Compans RW (1974) Characterization of temperature sensitive influenza virus mutants defective in neuraminidase. Virology 61: 397–410.
25. Shibata S, Yamamoto-Goshima F, Maeno K, Hanaichi T, Fujita Y, et al. (1993) Characterization of a temperature-sensitive influenza B virus mutant defective in neuraminidase. J Virol 67: 3264–3273.
26. Gubareva LV, Nedyalkova MS, Novikov DV, Murti KG, Hoffmann E, et al. (2002) A release-competent influenza A virus mutant lacking the coding capacity for the neuraminidase active site. J Gen Virol 83: 2683–2692.
27. Nedyalkova MS, Hayden FG, Webster RG, Gubareva LV (2002) Accumulation of defective neuraminidase (NA) genes by influenza A viruses in the presence of NA inhibitors as a marker of reduced dependence on NA. J Infect Dis 185: 591–598.
28. Lew W, Chen X, Kim CU (2000) Discovery and development of GS 4104 (oseltamivir): an orally active influenza neuraminidase inhibitor. Curr Med Chem 7: 663–672.

29. Fujii Y, Goto H, Watanabe T, Yoshida T, Kawaoka Y (2003) Selective incorporation of influenza virus RNA segments into virions. P Natl Acad Sci Usa 100: 2002–2007.
30. Shinya K, Fujii Y, Ito H, Ito T, Kawaoka Y (2004) Characterization of a neuraminidase-deficient influenza a virus as a potential gene delivery vector and a live vaccine. J Virol 78: 3083–3088.
31. Timpe JM, Stamataki Z, Jennings A, Hu K, Farquhar MJ, et al. (2008) Hepatitis C virus cell-cell transmission in hepatoma cells in the presence of neutralizing antibodies. Hepatology 47: 17–24.
32. Gupta P, Balachandran R, Ho M, Enrico A, Rinaldo C (1989) Cell-to-cell transmission of human immunodeficiency virus type 1 in the presence of azidothymidine and neutralizing antibody. J Virol 63: 2361–2365.
33. Pinto LH, Holsinger LJ, Lamb RA (1992) Influenza virus M2 protein has ion channel activity. Cell 69: 517–528.
34. Davies WL, Grunert RR, Haff RF, McGahen JW, Neumayer EM, et al. (1964) Antiviral Activity of 1-Adamantanamine (Amantadine). Science 144: 862–863.
35. Takeda M, Pekosz A, Shuck K, Pinto LH, Lamb RA (2002) Influenza a virus M2 ion channel activity is essential for efficient replication in tissue culture. J Virol 76: 1391–1399.
36. Chodosh J, Gan Y, Holder VP, Sixbey JW (2000) Patterned entry and egress by Epstein-Barr virus in polarized CR2-positive epithelial cells. Virology 266: 387–396.
37. Fuller S, von Bonsdorff CH, Simons K (1984) Vesicular stomatitis virus infects and matures only through the basolateral surface of the polarized epithelial cell line, MDCK. Cell 38: 65–77.
38. Schlie K, Maisa A, Freiberg F, Groseth A, Strecker T, et al. (2010) Viral protein determinants of Lassa virus entry and release from polarized epithelial cells. J Virol 84: 3178–3188.
39. Blau DM, Compans RW (1995) Entry and release of measles virus are polarized in epithelial cells. Virology 210: 91–99.
40. Brock SC, Goldenring JR, Crowe JE, Jr. (2003) Apical recycling systems regulate directional budding of respiratory syncytial virus from polarized epithelial cells. Proc Natl Acad Sci U S A 100: 15143–15148.
41. Roberts SR, Compans RW, Wertz GW (1995) Respiratory syncytial virus matures at the apical surfaces of polarized epithelial cells. J Virol 69: 2667–2673.
42. Tseng CT, Tseng J, Perrone L, Worthy M, Popov V, et al. (2005) Apical entry and release of severe acute respiratory syndrome-associated coronavirus in polarized Calu-3 lung epithelial cells. J Virol 79: 9470–9479.
43. Nayak DP, Hui EK, Barman S (2004) Assembly and budding of influenza virus. Virus Research 106: 147–165.
44. Carrasco M, Amorim MJ, Digard P (2004) Lipid raft-dependent targeting of the influenza A virus nucleoprotein to the apical plasma membrane. Traffic 5: 979–992.
45. Cresawn KO, Potter BA, Oztan A, Guerriero CJ, Ihrke G, et al. (2007) Differential involvement of endocytic compartments in the biosynthetic traffic of apical proteins. Embo J 26: 3737–3748.
46. Guerriero CJ, Lai Y, Weisz OA (2008) Differential sorting and Golgi export requirements for raft-associated and raft-independent apical proteins along the biosynthetic pathway. J Biol Chem 283: 18040–18047.
47. Kawaguchi A, Naito T, Nagata K (2005) Involvement of influenza virus PA subunit in assembly of functional RNA polymerase complexes. J Virol 79: 732–744.
48. Sugiura A, Ueda M, Tobita K, Enomoto C (1975) Further isolation and characterization of temperature-sensitive mutants of influenza virus. Virology 65: 363–373.
49. Guyader M, Kiyokawa E, Abrami L, Turelli P, Trono D (2002) Role for human immunodeficiency virus type 1 membrane cholesterol in viral internalization. J Virol 76: 10356–10364.
50. Jolly C, Sattentau QJ (2005) Human immunodeficiency virus type 1 virological synapse formation in T cells requires lipid raft integrity. J Virol 79: 12088–12094.
51. Phillips DM (1994) The role of cell-to-cell transmission in HIV infection. AIDS 8: 719–731.
52. Sato H, Orenstein J, Dimitrov D, Martin M (1992) Cell-to-cell spread of HIV-1 occurs within minutes and may not involve the participation of virus particles. Virology 186: 712–724.
53. Kawaguchi A, Momose F, Nagata K (2011) Replication-coupled and host factor-mediated encapsidation of the influenza virus genome by viral nucleoprotein. J Virol 85: 6197–6204.
54. Watanabe K, Handa H, Mizumoto K, Nagata K (1996) Mechanism for inhibition of influenza virus RNA polymerase activity by matrix protein. J Virol 70: 241–247.

THE JOURNAL OF BIOLOGICAL CHEMISTRY VOL. 286, NO. 38, pp. 33661–33668, September 23, 2011

Structures and Oxygen Affinities of Crystalline Human Hemoglobin C (β6 Glu→Lys) in the R and R2 Quaternary Structures*

Received for publication, May 29, 2011, and in revised form, July 17, 2011 Published, JBC Papers in Press, August 4, 2011, DOI 10.1074/jbc.M111.266056

Naoya Shibayama[‡1], **Kanako Sugiyama**[§], **and Sam-Yong Park**[§]

From the [‡]*Department of Physiology, Division of Biophysics, Jichi Medical University, 3311-1 Yakushiji, Shimotsuke, Tochigi 329-0498, Japan and the* [§]*Protein Design Laboratory, Yokohama City University, 1-7-29 Suehiro, Tsurumi, Yokohama 230-0045, Japan*

Recent crystallographic studies suggested that fully liganded human hemoglobin can adopt multiple quaternary conformations that include the two previously solved relaxed conformations, R and R2, whereas fully unliganded deoxyhemoglobin may adopt only one T (tense) quaternary conformation. An important unanswered question is whether R, R2, and other relaxed quaternary conformations represent different physiological states with different oxygen affinities. Here, we answer this question by showing the oxygen equilibrium curves of single crystals of human hemoglobin in the R and R2 state. In this study, we have used a naturally occurring mutant hemoglobin C (β6 Glu→Lys) to stabilize the R and R2 crystals. Additionally, we have refined the x-ray crystal structure of carbonmonoxyhemoglobin C, in the R and R2 state, to 1.4 and 1.8 Å resolution, respectively, to compare precisely the structures of both types of relaxed states. Despite the large quaternary structural difference between the R and R2 state, both crystals exhibit similar noncooperative oxygen equilibrium curves with a very high affinity for oxygen, comparable with the fourth oxygen equilibrium constant (K_4) of human hemoglobin in solution. One small difference is that the R2 crystals have an oxygen affinity that is 2–3 times higher than that of the R crystals. These results demonstrate that the functional difference between the two typical relaxed quaternary conformations is small and physiologically less important, indicating that these relaxed conformations simply reflect a structural polymorphism of a high affinity relaxed state.

Human hemoglobin, an $\alpha_2\beta_2$ tetrameric protein that exhibits strong cooperativity during oxygenation/deoxygenation, has long served as a model for understanding the structure-function relationships of allosteric proteins (1). For many years, the $\alpha_2\beta_2$ hemoglobin tetramer was though to adopt only two stable quaternary structures, the low affinity T (tense) and high affinity R (relaxed) structures, which are well suited to the notion of the Monod-Wyman-Changeux two-state allosteric model (2). This view was largely supported by crystallographic evidence that only one quaternary conformation (classical T structure) has so far been observed in a number of different crystals forms of human wild-type, mutant, and chemically modified deoxyhemoglobins (3–6). Likewise, the early crystallographic studies demonstrate that the structures of two independent fully liganded proteins, horse methemoglobin and human oxy (or carbonmonoxy) hemoglobin, assume essentially the same quaternary conformation (classical R structure) despite different crystal-packing contacts (7–9).

However, this simple view was challenged in the early 1990s by the discovery of a second relaxed state for fully liganded hemoglobin, known as R2 or Y, the quaternary structure of which is substantially different from that of the R state (10, 11). Computational studies suggest that R2 may be the relaxed end state in a T→R→R2 allosteric pathway, rather than an intermediate between T and R or an off-pathway intermediate (12). Also, recent NMR studies using ^{15}N-^{1}H residual dipolar couplings show that the quaternary conformation of human carbonmonoxyhemoglobin in solution is a dynamic ensemble of different quaternary structures that include the crystallographically identified R and R2 states (13). Consistent with this observation in solution, recent crystallographic studies identify previously unrecognized relaxed conformations that lie between R and R2 (14–16), although an additional liganded end state, R3, has also been proposed to exist (16). These recent findings strongly suggest that the fully liganded hemoglobin molecule is capable of traversing multiple conformations.

A basic question emerges as to whether R, R2, and other potential liganded conformations represent different physiological states with different oxygen affinities or whether they simply reflect a structural polymorphism of a high affinity relaxed state. To address this question directly, in this study we have determined the oxygen equilibrium curves of single crystals of human hemoglobin in the R and R2 quaternary structures by using absorption microspectrophotometry.

Previous microspectrophotometry studies on crystals of human deoxyhemoglobin in the T (tense) state demonstrated the feasibility of measuring the oxygen affinity of crystalline hemoglobin, opening up a new method for a direct comparison of the x-ray structure with its function in the same crystalline state (17, 18). However, so far this approach has not been applied to crystals of the fully liganded forms of hemoglobin, primarily because crystals of oxy (or carbonmonoxy) hemoglo-

* This work was in part supported by Grant-in-aid for Scientific Research 23570197 from the Japan Society for the Promotion of Science (to N. S.).

The atomic coordinates and structure factors (codes 3S65 and 3S66) have been deposited in the Protein Data Bank, Research Collaboratory for Structural Bioinformatics, Rutgers University, New Brunswick, NJ (http://www.rcsb.org/).

[1] To whom correspondence should be addressed. Tel.: 81-285-58-7308; Fax: 81-285-40-6294; E-mail: shibayam@jichi.ac.jp.

bin A in the R or R2 state shatter upon deoxygenation. Moreover, because those crystals are expected to have a high affinity for oxygen, they should be equilibrated with low oxygen pressures, requiring a very long experimental time. An additional difficulty is that the R2 crystals of hemoglobin A must be preserved under low pH conditions (below pH 6) (11), where the autooxidation rate is significantly increased. Here, we now show that the use of thin flat crystals of hemoglobin C (β6 Glu→Lys) in the R and R2 state can overcome most of these problems, thus enabling determination of their oxygen dissociation curves. It is known that hemoglobin C crystallizes much more readily than hemoglobin A due to the β6 Glu to Lys surface mutation, which makes the protein less soluble but does not significantly perturb the oxygen equilibrium properties (19–21). As a result, this mutant yields both R and R2 crystals of very high quality under mild conditions at neutral pH. Note that the use of thin crystals is, on the one hand, advantageous for shortening the experimental time, but, on the other hand, disadvantageous as to the signal to noise ratio of the absorption data. Thus, unlike previous measurements using oriented crystals and linearly polarized light (17, 18), we have used unpolarized light incident on horizontally oriented, thin flat crystals, to eliminate stray light reflected from the polarizer and to keep the signal to noise ratio as high as possible. In addition to the functional study, we have refined the crystal structure of carbonmonoxyhemoglobin C, in the R and R2 state, to 1.4 and 1.8 Å resolution, respectively. These high resolution data allow us to compare precisely the structures of both types of relaxed states, enabling discussion with the observed oxygen equilibrium curves of both states.

EXPERIMENTAL PROCEDURES

Preparation of Hemoglobin C—CS human blood was kindly obtained from Dr. Kazuhiko Adachi (The Children's Hospital of Philadelphia, Philadelphia, PA) and stripped as reported previously. The stripped hemoglobin sample was passed through a column of Sephadex G-25 equilibrated with CO-saturated 0.01 M phosphate buffer, pH 6.85, and then applied to a column of CM52 cellulose (Whatman) equilibrated with the same buffer. The column was washed with 2 column volumes of the same CO-saturated buffer, followed by 2 column volumes of the same buffer containing 0.2% (w/v) sodium dithionite ($Na_2S_2O_4$) to reduce (albeit the small amount of) methemoglobin in the original hemoglobin sample. After washing the column with 5 column volumes of the same CO-saturated buffer without dithionite, the column was eluted by a linear gradient of 0.01 M phosphate buffer, pH 7.15, and 0.04 M phosphate buffer, pH 7.60. The second major peak corresponding to hemoglobin C was collected and concentrated.

Crystallization and Structure Determination—Crystallization of carbonmonoxyhemoglobin C in the R state was carried out at 20 °C according to the batch method of Fitzgerald and Love (19), with some modifications, to give a CO-saturated 2.0% (w/v) hemoglobin solution containing 1.65 M phosphate buffer (0.528 M NaH_2PO_4 and 1.122 M K_2HPO_4, pH 7.2), 10% (v/v) glycerol, and 0.1% (w/v) D,L-homocysteine. A glass tube containing the above crystallization solution was placed into a gas-tight glass vial and quickly sealed under CO. Note that this vial also contained a small amount of Oxygen Absorbing System A-500HS (ISO, Yokohama, Japan) powder in its gas part, to maintain complete anaerobic conditions during crystallization. Similarly, crystals of carbonmonoxyhemoglobin C in the R2 state were obtained, using the same batch method at 20 °C, from CO-saturated 1.0% (w/v) hemoglobin solutions containing 11% (w/v) PEG 3350, 50 mM HEPES buffer, pH 7.6, and 10% (v/v) glycerol under complete anaerobic conditions. Both types of hemoglobin C crystals grew rapidly to their maximum dimensions within a few day. The mother liquors containing 15 and 20% (v/v) glycerol were used for the R and R2 crystals, respectively, as cryoprotectant in which the crystals were rinsed briefly before flash-freezing in liquid nitrogen.

X-ray data were collected using an ADSC Q270 CCD detector at beamlines BL17A and BL1A of the Photon Factory, Tsukuba, Japan. The wavelength of the incident x-rays was 1.0 Å. Diffraction datasets were processed with HKL2000 (22) and scaled with SCALEPACK (22). The R and R2 crystals belonged to the space group $P4_12_12$ and $P2_12_12_1$, respectively, with unit cell parameters of $a = b = 53.1$ Å, $c = 191.53$ Å, and $a = 57.78$ Å, $b = 58.75$ Å, $c = 172.87$ Å, respectively. Their structures were solved by molecular replacement using MOLREP (23, 24) and the previously reported structures of hemoglobin C (20, 21) (Protein Data Bank (PDB)[2] ID codes 1K1K and 1M9P) as a starting model. The best solution using data from 20 to 3.5 Å resolution range yielded a correlation coefficient of 0.55 and an R-factor of 0.40 for the R structure, and a correlation coefficient of 0.57 and an R-factor of 0.45 for the R2 structure, after rigid body refinement. At this stage, crystallographic refinement were pursued in PHENIX (25). After an initial round of simulated annealing refinement, several macrocycles that included bulk solvent correction, and anisotropic scaling of the data, individual coordinate refinement with minimization, and individual isotropic atomic displacement parameter refinement were carried out with maximum likelihood as the target. In the course of the refinement, water molecules were added to the models by manual inspection of their positions in both $2F_o - F_c$ and $F_o - F_c$ maps, and combined TLS (translation, libration, and screw-rotation) and individual atomic displacement parameter refinement were carried out in the final stages. Map fitting and other manipulations with molecular models were performed using the graphic software COOT (26). The stereochemistry of the final models of the R and R2 state (named R-COHbC and R2-COHbC, respectively) were assessed using PROCHECK (27). Data collection and refinement statistics are summarized in Table 1.

Oxygen Equilibrium Curves of Crystals—Crystals for oxygen equilibrium measurements were grown under the above mentioned conditions except for the absence of glycerol. Among grown crystals of various shapes, thin flat crystals were chosen

[2] The abbreviations used are: PDB, Protein Data Bank; K_4, fourth oxygen equilibrium constant; K_R, oxygen affinity of relaxed state; K_T, oxygen affinity of tense state; R-COHbA, 1.25 Å resolution crystal structure of carbonmonoxyhemoglobin A in the R state (PDB code 2DN3); R-COHbC, final structural model for carbonmonoxyhemoglobin C in the R state; R2-COHbC, the final structural model for carbonmonoxyhemoglobin C in the R2 state; r.m.s.d., root mean square deviation; T-deoxyHbA, the 1.25 Å resolution crystal structure of deoxyhemoglobin A in the T state (PDB code 2DN2).

TABLE 1
Crystal parameters, data collection, and structure refinement for the R and R2 crystals of human carbonmonoxyhemoglobin C

Dataset	R-COHbC	R2-COHbC
Data collection		
Resolution range (Å)	50.0–1.4	50.0–1.8
Space group	$P4_12_12$	$P2_12_12_1$
Unit cell dimensions (Å)	$a = 53.1$, $b = 53.1$, $c = 191.53$	$a = 57.78$, $b = 58.75$, $c = 172.87$
Reflections (Measured/Unique)	471,355/54,017	142,988/47,832
Completeness (%)	97.9 (91.8)[a]	86.4 (63.0)[a]
Mean $<I>/<\sigma(I)>$	18.0	24.6
Multiplicity	8.7	3.0
R_{merge} (%)[b]	3.4 (21.3)[a]	4.6 (60.1)[a]
B factor from Wilson plot (Å^2)	17	35
Refinement statistics		
Resolution range (Å)	20.0–1.4	20.0–1.8
R-factor (%)/free R-factor (%)[c]	20.8/23.3	25.0/30.5
R.m.s.d. from ideals		
Bond lengths (Å)	0.007	0.011
Bond angles (°)	1.079	1.486
No. of water molecules	208	47
Average B-factor (Hb/water, Å^2)	20/28	51/51
Ramachandran plot		
Residues in most favorable regions (%)	93.9	89.2
Residues in additional allowed regions (%)	6.1	10.0
Residues in generously allowed regions (%)	0.0	0.8

[a] The numbers in parentheses refer to the outer shell with a resolution of 1.45–1.4 Å and 1.86–1.8 Å for R-COHbC and R2-COHbC, respectively.
[b] $R_{merge} = \Sigma|I_i - <I_i>|/\Sigma|I_i|$, where I_i is the intensity of an observation and $<I>$ is the mean value for that reflection and the summations are overall reflections.
[c] R-factor $= \Sigma_h||F_o(h)| - |F_c(h)||/\Sigma_h F_o(h)$, where F_o and F_c are the observed and calculated structure factor amplitudes, respectively. The free R-factor was calculated with 5% of the data excluded from the refinement.

for measurements. Specifically, the R and R2 crystals used were hexagonal and trapezoidal in shape, respectively, each having a well developed (010) (or *ac*) crystal face. The crystals were washed with the mother liquors (0.8 M NaH_2PO_4 and 1.7 M K_2HPO_4 (pH 7.2) for the R crystals, and 25% (w/v) PEG 3350 and 50 mM HEPES (pH 7.6 or 7.2) for the R2 crystals) containing 0.1 mg of catalase/ml (Sigma).

For spectral measurements a single crystal with about 20 μl of its mother liquor was placed on a cover glass and then sealed into a flow chamber. Usually the settled crystal did not move during the measurements, because its well developed (010) face made good contact with the glass surface. The flow chamber was mounted on the stage of a Ziess UMSP 80 microspectrophotometer. Before measurements, removal of CO was carried out in the flow chamber with humidified oxygen, at a gas flow of 10 ml/min, under illumination of the white light of the microspectrophotometer. The time required for this conversion was <1 h, when small thin, flat crystals were used. Humidified nitrogen-oxygen gas mixtures at defined partial oxygen pressures were prepared by a GB-4C gas blender (Kofloc, Japan) with modifications and flowed into the chamber. The oxygen pressures were detected in the outflow from the chamber using a MC-7G-L galvanic O_2 sensor (Iijima, Japan). The absorption spectra of crystals equilibrated with different oxygen pressures at 21–22 °C were recorded between 450 and 700 nm with unpolarized light incident on (010) crystal face. According to the method of Mozzarelli *et al.* (17), the fractional saturation of the ferrous hemes with oxygen (Y) was calculated by a least square fit of the observed absorption spectra to a linear combination of three reference spectra and a base-line offset. The reference spectra are the absorption spectra of crystals of oxy-, deoxy-, and methemoglobin C. These spectra were determined on the same crystal as used for the oxygen equilibrium measurement. Because increases in oxygen pressure above 380 torr caused no appreciable spectral changes for the R or R2 crystals, the spectrum obtained under pure oxygen, after correction for the contribution from the methemoglobin content, was taken as the reference spectrum for oxyhemoglobin C. Note that the contribution from methemoglobin was removed by subtracting increasing amounts of the methemoglobin reference spectrum (see below) until the band at 630 nm disappeared. After each oxygen equilibrium measurement, the crystal was reduced by washing with mother liquor containing 0.2% (w/v) sodium dithionite ($Na_2S_2O_4$) for the measurement of the deoxyhemoglobin reference spectrum. In most cases the R and R2 crystals did not crack upon deoxygenation with dithionite. The crystal was then washed with mother liquor to remove sodium dithionite, followed by washing with mother liquor containing 5 mM potassium ferricyanide to oxidize the crystal for the measurement of the methemoglobin reference spectrum.

RESULTS AND DISCUSSION

X-ray Structures—At present, in the PDB the highest resolution data for the R and R2 structures of carbonmonoxyhemoglobin C are those of Hirsh and colleagues, determined at 2.0 and 2.1 Å resolution, respectively (20, 21) (PDB codes 1K1K and 1M9P). These resolutions are sufficient to be able to assign their quaternary structures but insufficient to make a precise comparison between their heme environmental structures. To improve this situation, we have undertaken the refinement of the crystal structures of carbonmonoxyhemoglobin C, in the R and R2 state, to 1.4 and 1.8 Å resolution, respectively (Table 1). In this study, the best crystals of the R and R2 state have been obtained under high salt conditions at pH 7.2 and low salt conditions at pH 7.6, respectively.

As summarized in Table 2, in both α and β subunits the proximal His(F8) geometries relative to the heme are very similar between R-COHbC and R2-COHbC and are similar to R-COHbA. Remarkably, in both subunits distances between the proximal His(F8) side chains and the hemes are virtually

TABLE 2
Stereochemical parameters for heme geometry and environment

Parameters	R-COHbC		R2-COHbC		T-deoxyHbA[a]		R-COHbA[a]	
	α	β	α1(α2)	β1(β2)	α	β	α	β
Distances to heme planes (Å)[b]								
Fe-P_{heme}	0.109	−0.060	0.199 (0.110)	−0.048 (−0.018)	0.646	0.562	0.107	−0.036
Fe-P_C	0.029	−0.026	−0.133 (0.048)	0.170 (0.207)	0.508	0.445	0.025	−0.002
His(F8) NE2-P_{heme}	2.206	2.054	2.275 (2.209)	2.082 (2.015)	2.82	2.728	2.207	2.077
Fe-ligand geometry								
Distances (Å)								
Fe-NE2(F8)	2.106	2.115	2.107 (2.131)	2.131 (2.094)	2.201	2.178	2.109	2.116
Fe–C(ligand)	1.734	1.772	1.766 (1.771)	1.771 (1.766)			1.736	1.711
C–O(ligand)	1.193	1.222	1.222 (1.220)	1.231 (1.223)			1.172	1.171
Angles (°)								
NE2(F8)–Fe–C(ligand)	177.3	175.4	175.9 (166.7)	175.7 (160.4)			179.3	175.0
Fe–C–O(ligand)	175.8	161.5	171.5 (142.7)	149.2 (141.2)			172.1	169.3
Distal ligand environment								
Distances (Å)								
His(E7)-Fe[c]								
NE2/CD2	4.4/5.2	4.5/5.2	5.4/6.6 (9.4 /9.3)	4.4/5.0 (4.6/5.3)	4.5/5.8	4.3/5.5	4.4/5.2	4.5/5.1
Val(E11)-Fe								
CG1/CG2	6.4/5.0	6.1/4.8	6.3/4.8 (5.7/4.9)	6.2/4.8 (6.2/4.9)	6.6/5.2	5.5/4.2	6.4/5.0	6.0/4.6
Phe(CD1)-Fe								
CZ	5.4	5.4	5.2 (5.2)	5.3/5.2	5.9	6.5	5.4	5.4

[a] T-deoxyHbA and R-COHbA are the 1.25 Å resolution crystal structures of T state deoxyhemoglobin A (PDB code 2DN2) and R state carbonmonoxyhemoglobin A (PDB code 2DN3), respectively (32).
[b] P_{heme} is the mean plane of porphyrin nitrogen atoms and carbon atoms plus first side chain (32 atoms), and P_C is the mean plane of the 20 porphyrin carbon atoms. The positive and negative values mean the directions from the heme plane toward the proximal and distal side, respectively.
[c] The distal His(E7) side chains are not so well ordered in the α2, β1, and β2 subunits in R2-COHbC (see "Results and Discussion").

identical in these relaxed conformations and shorter than T-deoxyHbA (Table 2), suggesting that the proximal strain, which is one of the key factors determining oxygen affinity, is relieved to a similar extent in R-COHbC, R2-COHbC, and R-COHbA. Also, in both subunits the distal ligand environments are in general similar between R-COHbC and R2-COHbC (Table 2). One exception is the distal His(E7), which appears to be positioned differently between R-COHbC and R2-COHbC (Fig. 1, *A–D* and Table 2). However, this disagreement cannot be considered significant because the distal His(E7) side chains are not so well ordered in the α2, β1, and β2 subunits in R2-COHbC, as indicated by the lack of well defined electron density map, whereas all other heme peripheral residues in R2-COHbC and those in R-COHbC (including Hisα58 and Hisβ63) are well ordered.

The observed dynamic behavior of His(E7) is not surprising because mutagenesis and kinetics studies show that the motilities of the distal His(E7) side chains are essential for opening a major channel for ligand entry in both hemoglobin subunits (28, 29). Also, crystallographic evidence for the His(E7) gate has recently been obtained for a new relaxed state of hemoglobin A at pH 6.4 (referred to here as RR3; PDB code 3D17), which shows a rotation of the β distal His(E7) out of the distal pocket, creating a direct channel to the bulk solvent (30). By contrast, so far there has been no crystallographic evidence for an opened ligand channel in human hemoglobin α subunits. This is probably because the α distal pocket is not so flexible as the β one, as predicted by the effects of mutagenesis (28, 29) and ligand size (31). Our data on R2-COHbC now suggest that the distal His(E7) in one of the α subunits (α2) is rather disordered but appears to rotate out of the distal pocket even at pH 7.6 (Fig. 1*C* and Table 2). The data also indicate that the distal His(E7) side chain in the α1 subunit is well ordered in a closed conformation, and both the β distal His(E7) side chains are similarly disordered.

We also investigated how the quaternary structures of R-COHbC and R2-COHbC are different from each other. Because the structure of the α1β1 dimer itself does not vary greatly among different states, the magnitude of the quaternary structural difference between two hemoglobin tetramers can be estimated by calculating the r.m.s.d. for the main-chain atoms between their α2β2 dimers after the corresponding α1β1 dimers are superimposed. We found that this r.m.s.d. value for R-COHbC and R2-COHbC is 4.95 Å, comparable with the r.m.s.d. value of 5.54 Å found for the deoxy T and carbonmonoxy R quaternary structures of hemoglobin A (32) (PDB codes 2DN2 and 2DN3). Analysis using difference distance matrix plots produced with *DDMP* (Center for Structural Biology, Yale University, New Haven, CT) confirmed that R-COHbC and R2-COHbC differ by the relative orientations of the α1β1 and α2β2 dimers in a way similar to that observed in the R and R2 structures of carbonmonoxyhemoglobin A (Fig. 1, *E* and *F*).

In crystals, the apparent oxygen saturation will depend on the heme orientation relative to the direction of the measuring light because the heme planes do not project equally onto the optical axis of the measuring light. Moreover, the heme orientation and crystal axes are different between the R and R2 crystals. Therefore, before oxygen equilibrium measurements, we should check the contributions made by the α and β hemes to light absorption in the R and R2 crystals. The R and R2 crystals used were hexagonal and trapezoidal in shape, respectively, each having a well developed (010) (or *ac*) crystal face. All of the spectra in this study were measured with light incident on this flat (010) crystal face. Based on the orientations of individual hemes in R-COHbC and R2-COHbC, the relative contributions of the individual hemes to the absorption could be calculated. A similar trend was found for both R and R2 crystals: The β hemes in the R and R2 crystals contribute 68 and 62%, respectively, of the total absorption. Thus, the measured oxygen affinities of the R and R2 crystals will be meaningfully compared with each

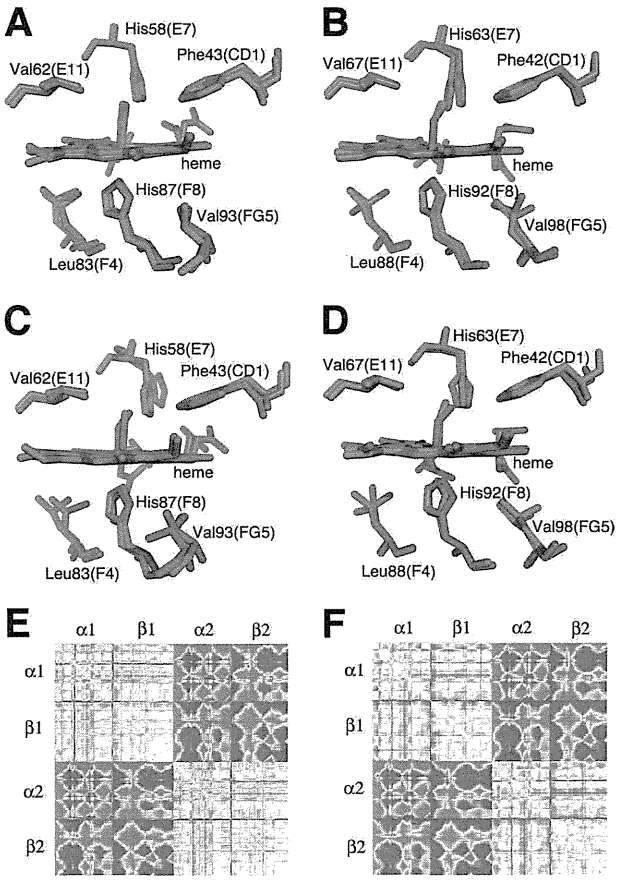

FIGURE 1. **Comparison between the R and R2 crystal structures of hemoglobin C.** *A*, stereoscopic comparison of the vicinity of the α1 heme between R-COHbC (*red*) and R2-COHbC (*blue*) by superimposing their α1 subunits. *B*, stereoscopic comparison of the vicinity of the β1 heme between R-COHbC (*red*) and R2-COHbC (*blue*) by superimposing their β1 subunits. *C*, stereoscopic comparison of the vicinity of the α2 heme between R-COHbC (*red*) and R2-COHbC (*blue*) by superimposing their α2 subunits. *D*, stereoscopic comparison of the vicinity of the β2 heme between R-COHbC (*red*) and R2-COHbC (*blue*) by superimposing their β2 subunits. *E*, difference distance matrix of R-COHbC and R2-COHbC. *F*, difference distance matrix of carbonmonoxyhemoglobin A in the R state (32) (PDB code 2DN3) and that in the R2 state (11) (PDB code 1BBB). In *E* and *F*, *blue* regions represent residues that move closer in the R structure, whereas the opposite happens in the *red* regions.

other, although both affinities are somewhat biased toward the affinity of the β heme.

Oxygen Equilibrium Properties—To make a direct comparison of the x-ray crystal structure with its function, crystals for oxygen equilibrium measurements were grown under the same conditions as for x-ray studies except for the absence of glycerol. Before oxygen equilibrium measurements, these crystals were converted to the oxy form by exposure to light and oxygen. Then, they were equilibrated with different oxygen pressures, and absorption spectra were recorded at 21–22 °C. The fractional saturation with oxygen was calculated by a least square fit of the observed absorption spectra to a linear combination of the reference spectra of the oxy-, deoxy-, and met- forms of the same crystal. These three reference spectra for an R crystal and those for an R2 crystal are present in Fig. 2, *A* and *B*, respectively. Typical time courses of deoxygenation experiments at an oxygen pressure of 0.857 torr, for the R and R2 crystals, are shown in Fig. 2, *C* and *D*, respectively. As evident from the comparison between Fig. 2, *C* and *D*, the oxygen affinity of the R2 crystals is higher than that of the R crystals, and the equilibration time required by the R2 crystals (<30 min) is much shorter than that by the R crystals (about 6 h) when comparing the crystals of similar thickness. It is currently unclear why the higher affinity R2 crystals require a shorter equilibration time (in general the reverse is true), but one interesting possibility is that the more flexible distal pockets observed in R2-COHbC could facilitate the ligand binding reaction in crystals. During these deoxygenation experiments, the methemoglobin contents of the R and R2 crystals were increased to 26 and 10%, respectively (see Fig. 2, *E* and *F*). However, previous study by Rivetti *et al.* (18) demonstrated that the fractional saturation with oxygen in crystals is independent of the presence of ferric hemes as long as the cooperativity is very small or absent. We below show that both crystalline samples actually meet this condition. Note that in this study only the data points in the upper 50% of fractional saturation could be collected because of the slow equilibration with oxygen, resulting from the very high oxygen affinity of the crystals. For example, as expected from Fig. 2*C*, the overall equilibration time of this crystal at an oxygen pressure below 0.2 torr would be longer than a day, making it difficult to obtain reliable data.

Hill plots of the oxygen dissociation curves for the R and R2 crystals of hemoglobin C are shown in Fig. 3*A*. Both Hill plots are linear, at least in the range above half-saturation, with slopes of close to unity. Specifically, the Hill coefficient, n, for the R and R2 crystals is 0.99 ± 0.03 and 1.04 ± 0.02, respectively, demonstrating the absence of cooperativity in oxygen binding by both relaxed quaternary conformations in the crystals. The reversibility of the oxygen binding was ensured by the agreement between the deoxygenation data and the corresponding oxygenation data. The oxygen pressure at half-saturation, P_{50}, for the R and R2 crystals is 0.29 ± 0.03 and 0.12 ± 0.01 torr, respectively, indicating that the R2 crystals have an ~2–3 times higher affinity for oxygen compared with that of the R crystals.

However, we should keep in mind that different solvent conditions used for the R and R2 crystals (*i.e.* high salt conditions at pH 7.2 for the R crystals, and low salt conditions at pH 7.6 for the R2 crystals) may affect differently the oxygen equilibrium properties of hemoglobin. Although both crystals are difficult to investigate under the same salt conditions, the adjustment of crystallization pH is much more feasible. Indeed, the R2 crystals grown at pH 7.2 were found to be isomorphous with those grown at pH 7.6 by determination of the unit cell parameters. Therefore, we determined the oxygen equilibrium curve of the R2 crystals grown at pH 7.2 to examine the effect of pH. As shown in Fig. 3*B*, the Hill plot of the oxygen equilibrium curve of the R2 crystals at pH 7.2 (n = 1.02 ± 0.03; P_{50} = 0.13 ± 0.01 torr) is very similar to that at pH 7.6, demonstrating that the difference in oxygen affinity between the R and R2 crystals is not due to the difference in pH. Note that although phosphate is known as an allosteric effector, available oxygen equilibrium data on hemoglobin A consistently show that the fourth oxygen equilibrium constant of human hemoglobin in solution (K_4) is almost insensitive to the phosphate concentration in the range

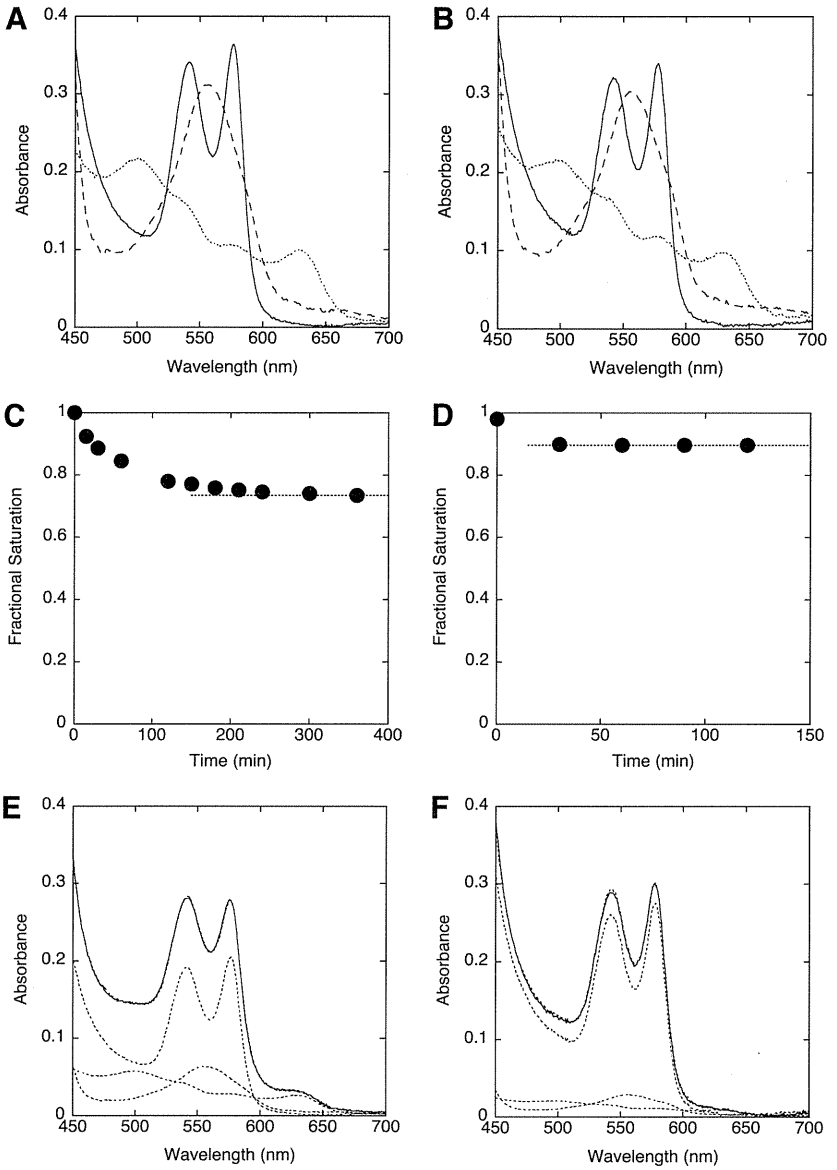

FIGURE 2. **Optical absorption spectra of crystalline hemoglobin C in the R and R2 quaternary structures.** Reference spectra of crystalline hemoglobin C, in the R and R2 state, are shown in *A* and *B*, respectively. In each panel, spectra of the oxy-, deoxy-, and methemoglobin are shown as *solid*, *dashed*, and *dotted line*, respectively. Typical time courses of deoxygenation experiments at an oxygen pressure of 0.857 torr for the R and R2 crystals, are shown in *C* and *D*, respectively. The fractional saturation of the ferrous hemes with oxygen (*Y*) was calculated by a least square fit of the observed absorption spectra to a linear combination of three reference spectra and a base-line offset. In *E*, the absorption spectrum of the R crystal equilibrated with oxygen at a pressure of 0.857 torr for 6 h is fitted with the reference spectra (*dotted line*). The fractional amounts of oxy-, deoxy-, and met- forms are calculated to be 54.6%, 19.7%, and 25.7%, respectively. In *F*, the absorption spectrum of the R2 crystal equilibrated with oxygen at a pressure of 0.857 torr for 2 h is fitted with the reference spectra (*dotted line*). The fractional amounts of oxy-, deoxy-, and met- forms are calculated to be 81.0%, 9.4%, and 9.6%, respectively.

of 0–0.1 M (33, 34). Thus, the evidence collected to date indicates that phosphate is an allosteric effector, which lowers the oxygen affinity of hemoglobin by shifting the allosteric equilibrium toward the T state and by lowering the oxygen affinity of the T state (K_T), but without changing the oxygen affinity of the R state (K_R) (34).

Our results do not provide information about functional heterogeneity between the α and β subunits. However, this does not affect our conclusions because, as already mentioned, the contributions made by the α and β hemes to apparent oxygen saturation are not so much different between the R and R2 crystals. Moreover, previous studies have shown that in solution the oxygen affinities of the α and β subunits within high affinity state hemoglobin are nearly identical (35, 36).

Interestingly, as shown in Fig. 3, the *dotted straight line* corresponding to the fourth oxygen equilibrium constant of human hemoglobin in solution (K_4 = 0.19 torr at 20 °C) (37) falls right in the middle between the Hill plots of the R and R2 crystals, suggesting that the oxyhemoglobin solution may contain nearly equal amounts of the R and R2 state. This is consis-

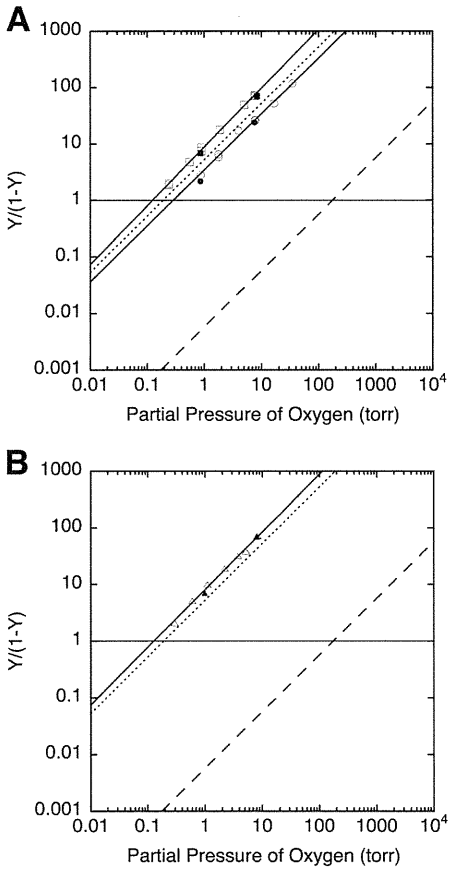

FIGURE 3. **Hill plots of the oxygen equilibrium curves of crystalline hemoglobin C in the R and R2 quaternary structures.** *A*, crystals of hemoglobin C in the R (*circles*) and R2 state (*squares*), which were suspended in 0.8 M NaH_2PO_4 and 1.7 M K_2HPO_4 (pH 7.2) and 25% (w/v) PEG3350 and 50 mM HEPES (pH 7.6), respectively, were equilibrated with either decreasing (*open symbols*) or increasing (*closed symbols*) oxygen pressures at 21–22 °C. *B*, crystals of hemoglobin C in the R2 state (*triangles*), which were suspended in 25% (w/v) PEG3350 and 50 mM HEPES (pH 7.2), were equilibrated with either decreasing (*open symbols*) or increasing (*closed symbols*) oxygen pressures at 21–22 °C. In each *panel*, the *solid lines* through data points represent the least squares fit of the deoxygenation data to the Hill equation. For comparison, the *dotted straight line* corresponding to the fourth oxygen equilibrium constant of human hemoglobin in solution (K_4 = 0.19 torr at 20 °C) (37) and the *dashed straight line* corresponding to the lowest affinity of solution deoxyhemoglobin (K = 175 torr at 20 °C) (37) are drawn.

tent with the previous NMR finding that the quaternary structure of carbonmonoxyhemoglobin A in solution is a dynamic intermediate between the energetically equivalent R and R2 crystal structures (13).

Previous x-ray crystallographic studies have identified a number of relaxed states of carbonmonoxyhemoglobin A, namely, R, R2, RR2, R3, and RR3, each of which has a distinct quaternary structure (8, 9, 11, 16, 30). It has been suggested that the R2 state may be the relaxed end state in a T→R→R2 allosteric pathway (12), and the RR2 state is an intermediate during the R→R2 transition (16). The R3 state, characterized by the smallest central water cavity among known conformations, has also been proposed as another relaxed end state in a T→R→R3 pathway (16). A recently discovered new relaxed state (referred to here as RR3) appears to lie in the pathway of the R→R3 transition (30, 38). Based on the different structural features at the central cavity and the β distal His(E7), Safo *et al.* have proposed that R, R2, R3 and other potential relaxed conformations represent different physiological states with different oxygen affinities, with R and R3 exhibiting the lowest and highest oxygen affinity, respectively (16, 30, 38). Until now, however, there is no direct functional evidence for, or against, this proposal.

Our study demonstrates that within single crystals both of the R and R2 states exhibit similar noncooperative oxygen equilibrium curves with a very high affinity for oxygen, comparable with the fourth oxygen equilibrium constant (K_4) of human hemoglobin in solution (Fig. 3). Accordingly, little change in oxygen affinity is expected to occur during the R→RR2→R2 transition. Although our data do not provide direct information on the R3 and RR3 states, we would like to point out that all of the oxygen affinities of other relaxed states, R, R2, and RR2, are very similar to the oxygen affinity of solution relaxed state (K_R) (34), which is an average over the ensemble of relaxed states existing in solution (such as R, R2, RR2, R3, and RR3). Therefore, it is unlikely that only the oxygen affinities of the R3 and RR3 states are substantially different from K_R, if these states are significantly populated under physiological conditions. Overall, we can conclude that the multiple relaxed conformations of fully liganded hemoglobin do not have a significant physiological role, but rather reflect interconvertible quaternary states all of which show a very high affinity for oxygen.

It is important to note here that the current success of determining the oxygen equilibrium curves of the R or R2 crystals is largely due to the use of hemoglobin C instead of hemoglobin A. Indeed, we found that deoxygenation of the R or R2 crystals of hemoglobin A caused irreversible behavior, presumably due to the occurrence of R-to-T transition. Increasing the concentration of the precipitant (phosphate or PEG) did not improve the reversibility, in contrast to the case of the T state crystals (18). We speculate that the precipitant displaces the hydration water from the hemoglobin molecule, which stabilizes the less hydrated T state but destabilizes the more hydrated R (or R2) state (39).

In summary, we have shown that, in crystals, both of the R and R2 structures exhibit similar noncooperative oxygen equilibrium curves with a very high affinity for oxygen, comparable with the K_4 of human hemoglobin in solution. Although the oxygen affinity of the R2 structure is 2–3 times higher than that of the R structure, this difference is energetically less important considering the entire affinity change of human hemoglobin (a 500–1000-fold change in oxygen affinity) (34, 37). More importantly, because both the affinities of the R and R2 structures are high enough to saturate hemoglobin with oxygen in the lungs, the oxygen transport activity of hemoglobin is not influenced by which conformation fully liganded hemoglobin adopts. Our high resolution x-ray data show that the heme environmental structure of the R state is not so much different from that of the R2 state despite the large quaternary difference between them. Altogether, these results indicate that multiple relaxed conformations of fully liganded hemoglobin do not play a physiological role in oxygen transport, but simply reflect a structural polymorphism of a high affinity relaxed state.

REFERENCES

1. Perutz, M. F. (1989) *Q. Rev. Biophys.* **22,** 139–237
2. Monod, J., Wyman, J., and Changeux, J. P. (1965) *J. Mol. Biol.* **12,** 88–118
3. Fermi, G., Perutz, M. F., Shaanan, B., and Fourme, R. (1984) *J. Mol. Biol.* **175,** 159–174
4. Kavanaugh, J. S., Rogers, P. H., Case, D. A., and Arnone, A. (1992) *Biochemistry* **31,** 4111–4121
5. Harrington, D. J., Adachi, K., and Royer, W. E., Jr. (1997) *J. Mol. Biol.* **272,** 398–407
6. Park, S. Y., Shibayama, N., Hiraki, T., and Tame, J. R. (2004) *Biochemistry* **43,** 8711–8717
7. Ladner, R. C., Heidner, E. J., and Perutz, M. F. (1977) *J. Mol. Biol.* **114,** 385–414
8. Baldwin, J. M. (1980) *J. Mol. Biol.* **136,** 103–128
9. Shaanan, B. (1983) *J. Mol. Biol.* **171,** 31–59
10. Smith, F. R., Lattman, E. E., and Carter, C. W., Jr. (1991) *Proteins* **10,** 81–91
11. Silva, M. M., Rogers, P. H., and Arnone, A. (1992) *J. Biol. Chem.* **267,** 17248–17256
12. Srinivasan, R., and Rose, G. D. (1994) *Proc. Natl. Acad. Sci. U.S.A.* **91,** 11113–11117
13. Lukin, J. A., Kontaxis, G., Simplaceanu, V., Yuan, Y., Bax, A., and Ho, C. (2003) *Proc. Natl. Acad. Sci. U.S.A.* **100,** 517–520
14. Mueser, T. C., Rogers, P. H., and Arnone, A. (2000) *Biochemistry* **39,** 15353–15364
15. Biswal, B. K., and Vijayan, M. (2001) *Curr. Sci.* **81,** 1100–1105
16. Safo, M. K., and Abraham, D. J. (2005) *Biochemistry* **44,** 8347–8359
17. Mozzarelli, A., Rivetti, C., Rossi, G. L., Henry, E. R., and Eaton, W. A. (1991) *Nature* **351,** 416–419
18. Rivetti, C., Mozzarelli, A., Rossi, G. L., Henry, E. R., and Eaton, W. A. (1993) *Biochemistry* **32,** 2888–2906
19. Fitzgerald, P. M., and Love, W. E. (1979) *J. Mol. Biol.* **132,** 603–619
20. Dewan, J. C., Feeling-Taylor, A., Puius, Y. A., Patskovska, L., Patskovsky, Y., Nagel, R. L., Almo, S. C., and Hirsch, R. E. (2002) *Acta Crystallogr. D Biol. Crystallogr.* **58,** 2038–2042
21. Patskovska, L. N., Patskovsky, Y. V., Almo, S. C., and Hirsch, R. E. (2005) *Acta Crystallogr. D Biol. Crystallogr.* **61,** 566–573
22. Otwinowski, Z., and Minor, W. (1997) *Methods Enzymol.* **276,** 307–326
23. Vagin, A., and Teplyakov, A. (2000) *Acta Crystallogr. D Biol. Crystallogr.* **56,** 1622–1624
24. Vagin, A. A., and Isupov, M. N. (2001) *Acta Crystallogr. D Biol. Crystallogr.* **57,** 1451–1456
25. Adams, P. D., Afonine, P. V., Bunkóczi, G., Chen, V. B., Davis, I. W., Echols, N., Headd, J. J., Hung, L. W., Kapral, G. J., Grosse-Kunstleve, R. W., McCoy, A. J., Moriarty, N. W., Oeffner, R., Read, R. J., Richardson, D. C., Richardson, J. S., Terwilliger, T. C., and Zwart, P. H. (2010) *Acta Crystallogr. D Biol. Crystallogr.* **66,** 213–221
26. Emsley, P., and Cowtan, K. (2004) *Acta Crystallogr. D Biol. Crystallogr.* **60,** 2126–2132
27. Laskowski, R. A., Moss, D. S., and Thornton, J. M. (1993) *J. Mol. Biol.* **231,** 1049–1067
28. Birukou, I., Schweers, R. L., and Olson, J. S. (2010) *J. Biol. Chem.* **285,** 8840–8854
29. Birukou, I., Soman, J., and Olson, J. S. (2011) *J. Biol. Chem.* **286,** 10515–10529
30. Jenkins, J. D., Musayev, F. N., Danso-Danquah, R., Abraham, D. J., and Safo, M. K. (2009) *Acta Crystallogr. D Biol. Crystallogr.* **65,** 41–48
31. Mims, M. P., Porras, A. G., Olson, J. S., Noble, R. W., and Peterson, J. A. (1983) *J. Biol. Chem.* **258,** 14219–14232
32. Park, S. Y., Yokoyama, T., Shibayama, N., Shiro, Y., and Tame, J. R. (2006) *J. Mol. Biol.* **360,** 690–701
33. Imai, K., and Yonetani, T. (1975) *J. Biol. Chem.* **250,** 2227–2231
34. Imai, K. (1982) *Allostric Effects in Haemoglobin,* Cambridge University Press, Cambridge
35. Unzai, S., Hori, H., Miyazaki, G., Shibayama, N., and Morimoto, H. (1996) *J. Biol. Chem.* **271,** 12451–12456
36. Unzai, S., Eich, R., Shibayama, N., Olson, J. S., and Morimoto, H. (1998) *J. Biol. Chem.* **273,** 23150–23159
37. Shibayama, N. (2011) in *Hemoglobin: Recent Developments and Topics* (Nagai, M., ed) pp. 138–140, Research Signpost, Kerala
38. Safo, M. K., Ahmed, M. H., Ghatge, M. S., and Boyiri, T. (2011) *Biochim. Biophys. Acta* **1814,** 797–809
39. Colombo, M. F., Rau, D. C., and Parsegian, V. A. (1992) *Science* **256,** 655–659

LETTER

doi:10.1038/nature10258

Crystal structure of the human centromeric nucleosome containing CENP-A

Hiroaki Tachiwana[1]*, Wataru Kagawa[1]*, Tatsuya Shiga[1]*, Akihisa Osakabe[1], Yuta Miya[1], Kengo Saito[1], Yoko Hayashi-Takanaka[2], Takashi Oda[3], Mamoru Sato[3], Sam-Yong Park[4], Hiroshi Kimura[2] & Hitoshi Kurumizaka[1]

In eukaryotes, accurate chromosome segregation during mitosis and meiosis is coordinated by kinetochores, which are unique chromosomal sites for microtubule attachment[1,2]. Centromeres specify the kinetochore formation sites on individual chromosomes, and are epigenetically marked by the assembly of nucleosomes containing the centromere-specific histone H3 variant, CENP-A[3–12]. Although the underlying mechanism is unclear, centromere inheritance is probably dictated by the architecture of the centromeric nucleosome. Here we report the crystal structure of the human centromeric nucleosome containing CENP-A and its cognate α-satellite DNA derivative (147 base pairs). In the human CENP-A nucleosome, the DNA is wrapped around the histone octamer, consisting of two each of histones H2A, H2B, H4 and CENP-A, in a left-handed orientation. However, unlike the canonical H3 nucleosome, only the central 121 base pairs of the DNA are visible. The thirteen base pairs from both ends of the DNA are invisible in the crystal structure, and the αN helix of CENP-A is shorter than that of H3, which is known to be important for the orientation of the DNA ends in the canonical H3 nucleosome[13]. A structural comparison of the CENP-A and H3 nucleosomes revealed that CENP-A contains two extra amino acid residues (Arg 80 and Gly 81) in the loop 1 region, which is completely exposed to the solvent. Mutations of the CENP-A loop 1 residues reduced CENP-A retention at the centromeres in human cells. Therefore, the CENP-A loop 1 may function in stabilizing the centromeric chromatin containing CENP-A, possibly by providing a binding site for *trans*-acting factors. The structure provides the first atomic-resolution picture of the centromere-specific nucleosome.

Octasome and hemisome models have been proposed for the CENP-A nucleosome architecture[14]. In the octasome model, two each of histones H2A, H2B, H4 and CENP-A form a histone octamer, and about 150 base pairs of DNA are wrapped in a left-handed orientation around the histone octamer, as in the canonical H3 nucleosomes[15–17]. In the hemisome model, however, one each of histones H2A, H2B, H4 and CENP-A[18,19] form a heterotypic tetramer, and the DNA is wrapped in a right-handed orientation around the tetramer[20].

To reveal the architecture of the CENP-A nucleosome, we prepared the nucleosome using bacterially expressed human histones H2A, H2B, H4 and CENP-A[16,21] (Supplementary Fig. 1) and a 147-base-pair palindromic DNA, which was designed from a human α-satellite sequence containing a binding site for the centromeric protein, CENP-B (Supplementary Fig. 2). The CENP-A nucleosome was reconstituted by a salt-dialysis method, and crystallized as described (Supplementary Methods). The structure was determined at 3.6 Å resolution (Fig. 1, Supplementary Table 1). The crystal structure revealed a histone octamer containing two each of histones H2A, H2B, H4 and CENP-A, with the DNA wrapped in a left-handed orientation around the histone octamer

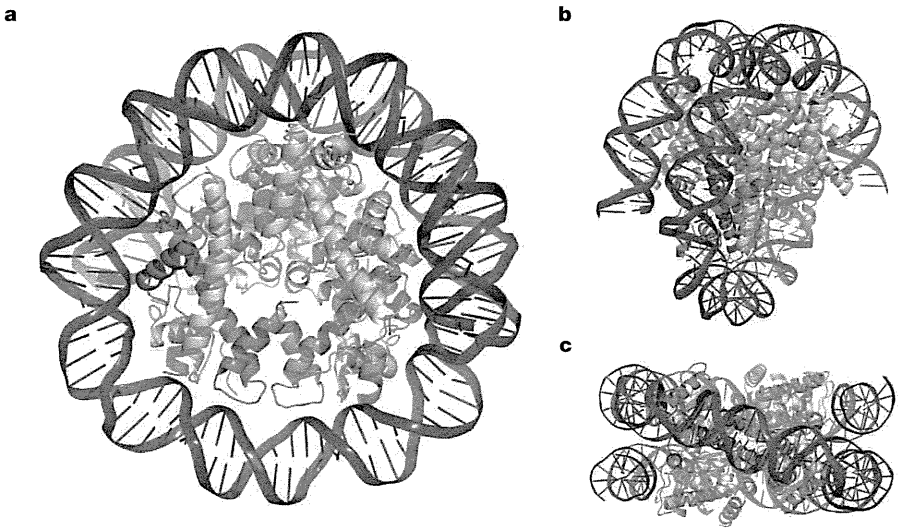

Figure 1 | Crystal structure of the human CENP-A nucleosome. a–c, Three views of the CENP-A nucleosome structure are presented. **a**, View in the axis of the DNA supercoil; **b**, **c**, views from the side of the DNA supercoil. Two CENP-A molecules are shown in magenta and green, respectively. The central 121-base-pair DNA region, which is visible in the CENP-A nucleosome structure, is shown in dark blue.

[1]Laboratory of Structural Biology, Graduate School of Advanced Science and Engineering, Waseda University, 2-2 Wakamatsu-cho, Shinjuku-ku, Tokyo 162-8480, Japan. [2]Graduate School of Frontier Biosciences, Osaka University, 1-3 Yamada-oka, Suita, Osaka 565-0871, Japan. [3]Division of Macromolecular Crystallography, Department of Supramolecular Biology, Graduate School of Nanobioscience, Yokohama City University, 1-7-29 Suehiro-cho, Tsurumi, Yokohama 230-0045, Japan. [4]Protein Design Laboratory, Department of Supramolecular Biology, Graduate School of Nanobioscience, Yokohama City University, 1-7-29 Suehiro-cho, Tsurumi, Yokohama 230-0045, Japan.
*These authors equally contributed to this work.

(Fig. 1). The overall structure is quite similar to those of previously solved nucleosomes containing other histone H3 variants[13,22,23]. The left-handed DNA wrapping in the crystal structure was also observed in biochemical experiments. CENP-A oligonucleosomes assembled on circular plasmid DNA by a salt-dialysis method or in the presence of human histone chaperones, NAP1 and somatic nuclear autoantigenic sperm protein (sNASP)[24,25], under physiological salt conditions, introduce left-handed (negative) supercoils in the DNA (Supplementary Figs 3 and 4). These results strongly indicate that the DNA wrapped in a left-handed orientation is the predominant form in the human CENP-A nucleosome.

In the free CENP-A–H4 structure reported previously[26], the CENP-A–CENP-A interface is substantially rotated relative to the H3–H3 interface, indicating that the CENP-A–H4 tetramer may be more compact than the H3–H4 tetramer. However, this specific shape of the CENP-A–CENP-A interface may only be observed in the free CENP-A–H4 tetramer, because the CENP-A–CENP-A interface in the present structure was nearly identical to that of the H3–H3 interface in the canonical H3 nucleosome. Consistently, small-angle X-ray scattering (SAXS) measurements of CENP-A and H3 nucleosomes generated nearly identical SAXS curves and distance distribution functions (Supplementary Fig. 5). These results indicate that the global structures of the CENP-A and H3 nucleosomes are quite similar. In addition, a compact CENP-A nucleosome model containing 147 base-pair DNA constructed from the free H3–H4 tetramer structure[26] generated a significantly different SAXS curve and distance distribution function from those of a CENP-A nucleosome model containing 147 base pair DNA based on the CENP-A nucleosome crystal structure, which was very similar to the experimental data (Supplementary Fig. 6). Therefore, the CENP-A nucleosome structure is probably not compacted as was suggested previously[26].

Although the overall structure of the CENP-A nucleosome resembles that of the canonical H3 nucleosome, in the CENP-A nucleosome structure, only the central 121 base pairs of the DNA are visible, and thus the thirteen base pairs from both ends of the DNA are disordered (Fig. 1 and Supplementary Fig. 7). This observation indicates that the DNA regions at the entrance and exit of the CENP-A nucleosome lack a fixed conformation. This is consistent with the previous report showing that the DNA segments at the entrance and exit of the CENP-A nucleosome are more flexible than those of the canonical H3 nucleosome[26–28]. We found that the CENP-A nucleosome can be reconstituted on a 121 base pair DNA (Supplementary Fig. 8). The CENP-A nucleosome induced supercoils into plasmid DNA less efficiently than the H3 nucleosome, which also indicates that the DNA is partially unwrapped in the CENP-A nucleosomes (Supplementary Fig. 9). Furthermore, the exonuclease assay revealed that the DNA ends of the CENP-A nucleosomes were more susceptible to exonuclease III digestion, compared to those of the H3 nucleosome (Supplementary Fig. 10). Similar results were obtained with other DNA sequences without the CENP-B box (Supplementary Fig. 10). Moreover, the SAXS data showed that the maximum dimension D_{max} (D_{max} = 165 Å) of the CENP-A nucleosome is slightly longer than that of the H3 nucleosome (D_{max} = 147 Å), which probably reflects the unwrapped conformations of the thirteen base pairs from both ends of the DNA in the CENP-A nucleosome (Supplementary Fig. 5).

This difference in the DNA end structures can be explained by the structural differences between the amino-terminal regions of CENP-A and H3 (Fig. 2a). Previous crystal structures of the canonical H3 nucleosome revealed that the loop segment preceding the αN helix of H3 interacts with the ends of the DNA, and seems to stabilize their orientations (Fig. 2b)[13,22,23]. Thus, the length of the αN helix seems to be an important factor for maintaining the DNA orientation at the entrance and exit of nucleosomes. The αN helix of CENP-A is at least one helical turn shorter than that of H3, and the preceding region is completely disordered (Fig. 2b). The DNA conformations at the entrance and exit of the nucleosome are clearly related to the organization of the nucleosomes[29], particularly within the heterochromatin, where the nucleosomes are presumably tightly packed. A previous study indicated that the centromeric DNA binding protein, CENP-B, binds efficiently to its recognition sequence[30], if the sequence is located near the entrance or exit of the CENP-A nucleosome[16]. The flexible nature of both ends of the DNA in the CENP-A nucleosome structure may be an inherent property that facilitates the binding of CENP-B, and possibly other centromeric DNA-binding proteins. Thus, the αN helix of CENP-A may have a key role in allowing the DNA to adopt the specific conformations at the entrance and exit of the nucleosome, which are not observed in the canonical H3 nucleosome.

It is notable that CENP-A–DNA contacts may exist at the flexible DNA ends of the CENP-A nucleosome. In the exonuclease digestion experiments (Supplementary Fig. 9), we observed DNA fragments longer than 121 base pairs, suggesting that the CENP-A–DNA contacts may extend beyond 121 base pairs of DNA. Furthermore, the CENP-A nucleosome reconstitution efficiency was slightly lower with a 121-base-pair DNA, compared to that with a 147-base-pair DNA (Supplementary Fig. 8). A possible interpretation is that the CENP-A–DNA contacts extending beyond 121 base pairs of DNA may stabilize

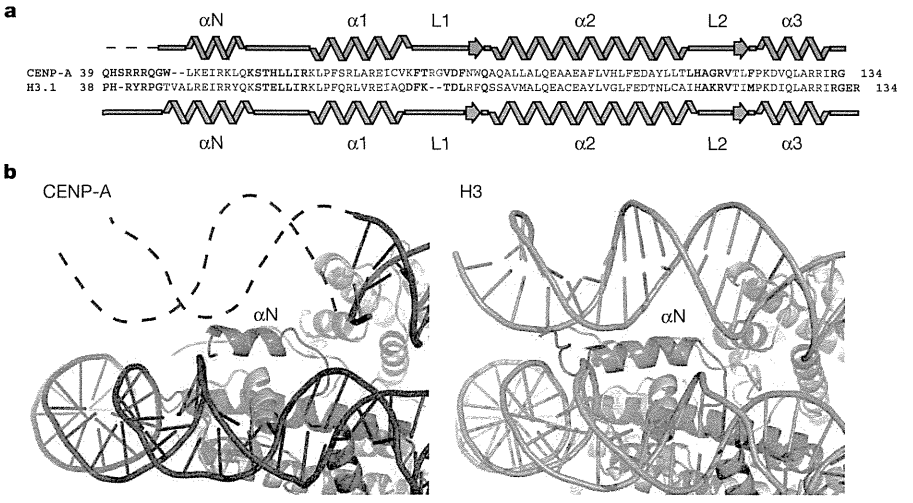

Figure 2 | Structure of the DNA entrance and exit of the human CENP-A nucleosome. **a**, Secondary structure of CENP-A in the nucleosome. The sequences of human CENP-A and H3 are aligned with the secondary structure elements. **b**, Close-up views of the αN helices and the DNA edge regions of the CENP-A (left panel) and H3 (right panel) nucleosomes. The dashed line in the left panel shows the DNA region that is not visible in the crystal structure. The CENP-A and H3 molecules are shown in magenta and orange, respectively.

the CENP-A nucleosome, resulting in higher reconstitution efficiencies on a 147-base-pair DNA.

A superimposition of CENP-A and H3 reveals a clear difference in the loop 1 region (residues Phe 78–Phe 84 of CENP-A), where CENP-A has two extra amino acid residues (Arg 80 and Gly 81) compared to H3 (Fig. 2a). The CENP-A loop 1 protrudes from the CENP-A nucleosome, and the Arg 80 and Gly 81 residues are located at the tip of the loop (Fig. 3 and Supplementary Fig. 11). In the free CENP-A–H4 tetramer structure, the loop 1 region is more flexible than the other CENP-A regions, as judged from the B-factors. By contrast, in the CENP-A nucleosome, the B-factors of the loop 1 region are similar to those of the other regions (Supplementary Fig. 12), indicating that CENP-A nucleosome formation may stabilize the loop 1 region. The tip of the loop 1 region is solvent-accessible (Fig. 3), and may function as a binding site for *trans*-acting factors that interact directly with the CENP-A nucleosome. To test the functional significance of the CENP-A Arg 80 and Gly 81 residues, we co-expressed the green fluorescent protein (GFP)-tagged CENP-A and the red fluorescent protein (RFP)-tagged CENP-A(del), in which the Arg 80 and Gly 81 residues were deleted, in human-telomerase-immortalized retina pigment epithelial (hTERT-RPE1) cells. Within 1 or 2 days after transfection, both GFP-tagged CENP-A and RFP-tagged CENP-A(del) were recruited to the centromeres, which were identified by a constitutive centromere protein, CENP-C (Fig. 4a). This result indicates that the Arg 80 and Gly 81 residues are not essential for targeting CENP-A to the centromeres. However, 3 days after transfection, the number of cells in which the CENP-A(del) signals were detected at the centromeres was markedly reduced (Fig. 4b). Concomitantly, the number of cells with the CENP-A signal alone increased (Fig. 4b). Similar results were obtained when the fluorescent labels were swapped between CENP-A and CENP-A(del), showing that the phenomenon does not depend on the fusion partner (Fig. 4c). These results indicate that CENP-A(del) is less stably incorporated into centromeres, compared to CENP-A. In addition, two CENP-A mutants, one containing the Arg 80-Gly 81 to Ala 80-Ala 81 substitution (CENP-A(A80A81)) and another with the Val 82-Asp 83 deletion, which disrupts the Arg 80-Gly 81 protrusion (CENP-A(del82-83)), were targeted to centromeres at levels comparable to those of CENP-A, 1 day after transfection. The number of cells retaining the CENP-A mutants at the centromeres also decreased, 3 days after transfection (Supplementary Fig. 13a, b). However, like CENP-A, the CENP-A mutant containing the Val 82-Asp 83 to Ala82-Ala83 substitution (CENP-A(A82A83)) remained at the centromeres, 3 days after transfection (Supplementary Fig. 13c). Thus, the Arg 80 and Gly 81 residues and the size of the protruding loop 1 are critical for stable CENP-A retention at centromeres.

There has been much debate over the CENP-A nucleosome structure and its role in the centromere-specific chromatin structure. Because CENP-A has lower sequence homology to H3, compared to

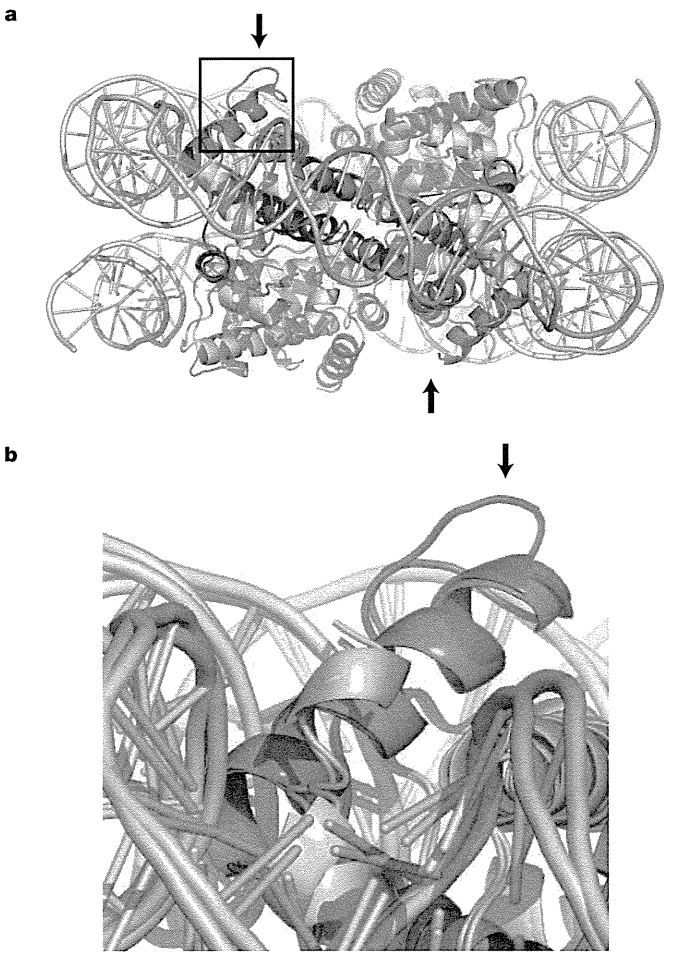

Figure 3 | Structural differences in the loop 1 regions between CENP-A and H3. **a**, Side view of the CENP-A nucleosome. The CENP-A molecules are shown in magenta and green. The box indicates the region enlarged in panel **b**. **b**, Superimposition of the CENP-A (magenta) and H3 (orange) loop 1 regions. Arrows indicate the tip of the CENP-A loop 1 containing the Arg 80 and Gly 81 residues.

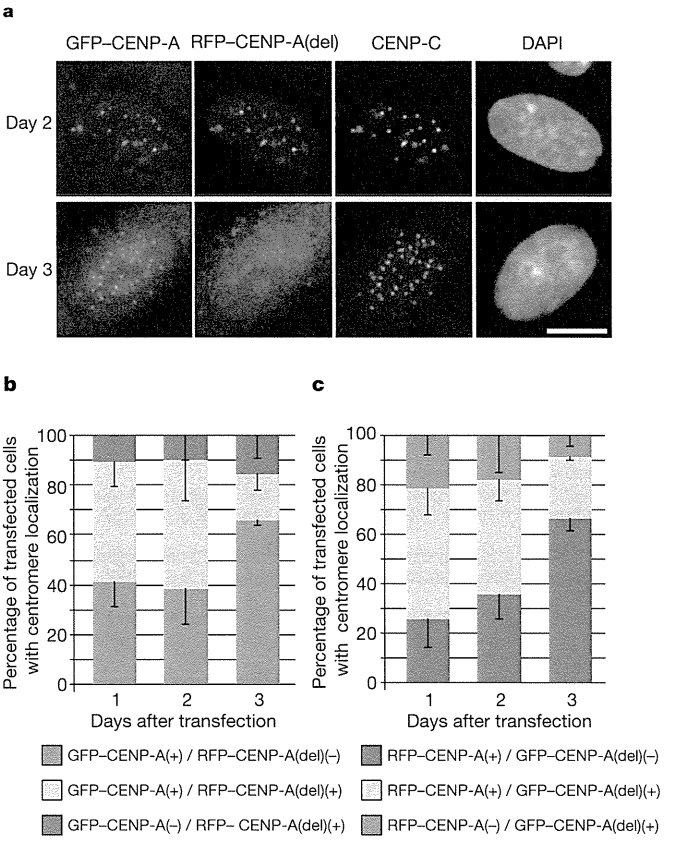

Figure 4 | Less stable association of CENP-A(del) with the centromere. **a**, Fluorescence images. hTERT-RPE1 cells were transfected with GFP-tagged CENP-A and RFP-tagged CENP-A(del), fixed, and stained with anti-CENP-C (Cy5) and DAPI. Bar, 10 μm. **b**, Quantitative data. Using images such as those in panel **a**, the numbers of transfected hTERT-RPE1 cells showing GFP–CENP-A, RFP–CENP-A(del), or both at centromeres were counted ($n > 28$), and the average percentages from three independent transfections were plotted with the standard deviations. **c**, hTERT-RPE1 cells were transfected with GFP-tagged CENP-A(del) and RFP-tagged CENP-A, and were analysed as described in panel **b** ($n > 20$).